Journal Pre-proof

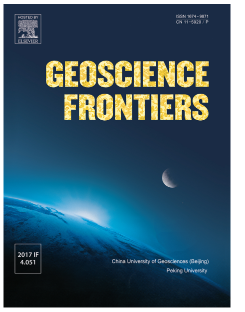

Scattering and absorption imaging of a highly fractured fluid-filled seismogenetic volume in a region of slow deformation

Ferdinando Napolitano, Luca De Siena, Anna Gervasi, Ignazio Guerra, Roberto Scarpa, Mario La Rocca

PII: S1674-9871(19)30199-9

DOI: https://doi.org/10.1016/j.gsf.2019.09.014

Reference: GSF 899

To appear in: *Geoscience Frontiers*

Received Date: 23 January 2019

Revised Date: 27 July 2019

Accepted Date: 29 September 2019

Please cite this article as: Napolitano, F., De Siena, L., Gervasi, A., Guerra, I., Scarpa, R., La Rocca, M., Scattering and absorption imaging of a highly fractured fluid-filled seismogenetic volume in a region of slow deformation, *Geoscience Frontiers*, https://doi.org/10.1016/j.gsf.2019.09.014.

***Declaration of Interest Statement**

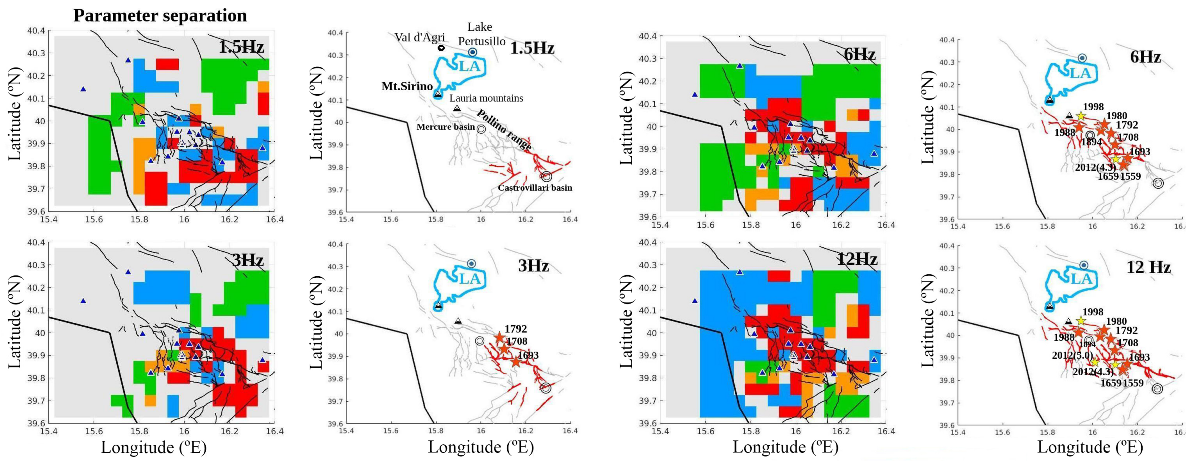

Parameter separation
1.5Hz
3Hz
6Hz
12Hz
12 Hz
Val d'Agri
Lake
Pertusillo
LA
Mt.Sirino
Lauria mountains
Mercure basin
Pollino range
Castrovillari basin
1998
1980
1792
1988
1708
1693
2012(4.3)
2012(5.0)
1659
1559
Latitude (°N)
Longitude (°E)

Scattering and absorption imaging of a highly fractured fluid-filled seismogenetic volume in a region of slow deformation

Ferdinando Napolitano[a], Luca De Siena[b,c], Anna Gervasi[d,e], Ignazio Guerra[d], Roberto Scarpa[a], Mario La Rocca[d]

[a]*Dipartimento di Fisica "E.R. Caianiello", Università degli Studi di Salerno, Via Giovanni Paolo II, 84084, Fisciano (SA), Italy.* ***email to:*** *fnapolitano@unisa.it*
[b]*Institute of Geosciences, Johannes Gutenberg University Mainz, J.-J.-Becher-Weg 21, D-55128 Mainz, Germany*
[c]*University of Aberdeen, School of Geosciences, Geology and Petroleum Geology, Meston Building, King's College, Aberdeen AB24 3UE Scotland, UK*
[d]*Dipartimento di Biologia, Ecologia e Scienze della Terra, Università della Calabria, Ponte P. Bucci, 87036, Arcavacata di Rende (CS), Italy*
[e]*Istituto Nazionale di Geofisica e Vulcanologia, Sezione di Rende (CS), Ponte P. Bucci, 87036, Arcavacata di Rende (CS), Italy*

Abstract

Regions of slow strain often produce swarm-like sequences, characterized by the lack of a clear mainshock-aftershock pattern. The comprehension of their underlying physical mechanisms is challenging and still debated. We used seismic recordings from the last Pollino swarm (2010-14) and nearby to separate and map seismic scattering (from P peak-delays) and absorption (from late-time coda-wave attenuation) at different frequencies in the Pollino range and surroundings. High-scattering and high-absorption anomalies are markers of a fluid-filled fracture volume extending from SE to NW (1.5-6 Hz) across the range. With increasing frequency, these anomalies approximately cover the area where the strongest earthquakes occurred from the sixteenth century until 1998. In our interpretation, the NW fracture propagation ends where carbonates of the Lucanian Apennines begin, as marked by a high-scattering and low-absorption area. At the highest frequency (12 Hz) the anomalies widen southward in the middle of the range, consistently marking the faults active during the recent Pollino swarm. Our results suggest that fracture healing has closed small-scale fractures across the SE faults that were active in the past centuries, and that the propagation of fluids may have played a crucial role in triggering the 2010-2014 Pollino swarm. Assuming that the fluid propagation ended at the carbonates barrier in the NW direction, fractures opened new paths to the South, favoring the nucleation of the last Pollino swarm. Indeed, the recently active faults in the middle of the seismogenic volume are marked by a high-scattering and high-absorption footprints. Our work provides evidence that attenuation parameters may track shape and dynamics of fluid-filled fracture networks in fault areas.

Keywords: Pollino, seismic attenuation, scattering, fluids, fractures, healing.

1. Introduction

The southern Apennines and the Calabrian arc are among the most seismically-active areas of the Mediterranean region. Despite the intense seismic activity, gaps in historical documentation (Scionti et al., 2006) and the low population density of the area (Cinti et al., 1997) have marked the Pollino range as a "seismic gap" between the southern Apennine and the Crati Valley (Rovida et al., 2011; Tertulliani and Cucci, 2014) (Figure 1). Paleoseismological investigations show clear evidence of large-magnitude earthquakes (M6.5-7) occurred along two seismogenic areas, the Pollino and

Castrovillari faults (POL and CAS in Figure 1) (Cinti et al., 1997, 2002). A few earthquakes of moderate magnitude occurred during seismic sequences struck these areas in the past centuries, as the 1693 Pollino seismic sequence (Tertulliani and Cucci, 2014) or the 1708 earthquake (M5.5). In 1998, a $m_L = 5.0$ earthquake occurred in the Mercure basin, northwest of the Pollino massif, triggering the Pollino-Mercure basin sequence (Guerra et al., 2005). Although the uncertainties on the location of historical events are higher than for recent seismicity, there is evidence of a migration of the seismogenic volumes from SE to NW across the Pollino range between 1559 and 2014 (Figure 1). Between 2010 and 2014 a sequence of almost 10.000 earthquakes of small-to-moderate magnitude with two mainshocks of $M_L 4.3$ and $M_L 5.0$ occurred in the Pollino area (Totaro et al., 2015; Passarelli et al., 2015) (Figures 1-2). During this sequence, characterized by a migration in time from NW toward SE (Fig. 1), a slow-slip event lasting several months (between 2012 and 2013) was detected in the same area via the GPS monitoring network (Cheloni et al., 2017). Seismic data have been used in combination with geological and remote-sensing data to map seismically-active normal faults Brozzetti et al. (2017) and to evaluate local site effects (Napolitano et al., 2018) in the area. The relationship between slow-strain areas, often characterized by a combination of seismic brittle failures and aseismic slip, and swarm-like seismic activity is one of the possible scenarios proposed, e.g., by Lohman and McGuire (2007); Peng and Gomberg (2010); Passarelli et al. (2015). Even though the correlation between swarm-like activity and their fault mechanisms is not fully understood, these works suggest that aseismic processes are a general and common feature driving swarm-like sequences.

For this reason, novel geophysical imaging is necessary to improve hazard estimation for earthquakes that, in slow-strain regions, are episodic and spatially migrating (Landgraf et al., 2017).

Seismic attenuation tomography has the potential to image the extension of highly-fractured volumes, especially when fluids saturate them inducing seismicity (De Siena et al., 2016, 2017; Amoroso et al., 2017). The two physical mechanisms that induce inelastic attenuation while a wave travels through the crust are seismic scattering and absorption. The introduction of the radiative transfer equation solved by numerical Monte Carlo simulations put forward the important role of multiple scattering in the generation of coda waves (Paasschens, 1997; Sato et al., 2012). In their seminal paper, Gusev and Abubakirov (1999) devise a strategy to invert the broadening envelopes (the seismic intensities recorded at a station, Fig. 3) for transport turbidity, a single parameter describing scattering attenuation and back-scattering of coda waves. At crustal scale, the peak-delay time (i.e. the time lag from the direct-wave onset to the maximum amplitude of the signal envelope) is generally considered a direct measure of multiple forward scattering after correcting for path-propagation (Saito et al., 2002; Takahashi et al., 2007; Calvet and Margerin, 2013).

Coda waves (the later portion of the seismogram) are the main manifestation of the redistribution of seismic energy caused by multiple scattering. Their attenuation (Q_c^{-1}) is measured from the exponential decay of coda energy envelopes with time (Aki and Chouet, 1975). At long lapse times and in a uniform anisotropic half-space, coda waves theoretically enter the diffusive regime, which in turn implies equality between coda attenuation and absorption (Shapiro et al., 2000). This assumption is valid at regional scale for seismicity constrained in the crust, i.e. in a thick layer regime (Calvet et al., 2013; Margerin, 2017) - which in turn means that earthquakes are mostly constrained inside a thick ($\leq 30km$) crust. At late lapse times, coda waves from these earthquakes have undergone multiple scattering interactions: equipartition between P- and S-waves (Hennino et al., 2001) is considered a good marker of the diffusion regime in this setting. Calvet and Margerin (2013) demonstrate that coda-wave attenuation at t_W= 80 s is a measurement of seismic absorption for epicentral distances between 0 and 90 km in the Pyrenees. Borleanu et al. (2017) use a similar assumption to image Vrancea (Romania), revealing extension and shape of sedimentary basins. The joint use of peak-delays and Q_c^{-1} in a thick crust like the Pollino area (average Moho depth at 45km) thus allows to separate scattering attenuation from absorption.

Q_c^{-1} regionalisation can reconstruct the geotectonic characteristics of seismogenic regions (eg Ugalde et al., 2002). Nevertheless, while peak-delays are sensitive to a tight area around the seismic rays (Saito et al., 2002), assigning Q_c^{-1} to ray paths between source and receiver is inaccurate (Del Pezzo et al., 2016). Also, the regionalisation approach hinders testing of anomalies as it does not use a proper forward model for inversion. Recently, modelling of coda amplitude through kernel functions has been proposed (Margerin et al., 2015; Del Pezzo et al., 2016) and tested (Mayor et al., 2016; De Siena et al., 2017) at crustal and local (volcanic) scales. Most of these functions are computed via a Monte Carlo numerical simulation of the Energy Transport Equation. With the above-mentioned assumptions, the multiple anisotropic scattering process leads to diffusion in a time-window where equipartition takes place (Hennino et al., 2001; Souriau et al., 2011) and in the absence of leakage and strong boundary conditions (De Siena et al., 2013; Margerin, 2017). All studies agree that in this case the functions have two maxima at source and station positions and expand around them depending on the average scattering properties of the medium (eg Obermann et al., 2013; Del Pezzo et al., 2016).

We used earthquakes of the 2010-2014 Pollino sequence and crustal earthquakes recorded in the surrounding area [lon: 15.4, 16.4; lat: 39.6, 40.4] to produce 2D maps showing the spatial variations of peak-delay time and Q_c^{-1}. While we regionalized peak-delay measurements, we used an analytic approximation of the diffusive sensitivity kernels (Del Pezzo et al., 2016) to model the effective amplitude decrease of coda waves at late lapse times, and inverted Q_c^{-1} in space (De Siena et al., 2017). We tested the resolution and reliability of the final results by inverting on grids having different steps, changing damping parameters and performing checkerboard tests. We use these maps as a proxy of the lateral variations of seismic scattering and absorption in the Pollino area, allowing us to image fault structures, fracture networks, and their influence on fluid propagation and seismicity between the 16th century and today.

2. Geological and geophysical settings

The Pollino area (Southern Italy) is a transition zone between the Southern Apennines NE-verging collision and the Calabrian rollback subduction zone. Located on the northern side of the Calabrian fore-arc and accretionary wedge, it is a striking example of the faster subduction (relative to the normal subduction in the Mediterranean) of the African under the European plate (Faccenna et al., 1996). The Calabrian fore-arc collided with the continental margins of Nubia, forming the Maghrebides, and of Apulia, forming the Apennines. Two shallow tectonic units coexist in the Pollino transition zone: 1) the allochthonous *Liguride Unit*, representing the remnants of the northern continental margin of Neotethys (Cello et al., 1996) and 2) the *Apennines Platform*, a thick carbonate shelf succession represented by the Verbicaro Unit overlaying the Pollino Unit. Furthermore, in the Campotenese area, the superposition of the Verbicaro unit onto the Campotenese-Pollino unit is marked by a ductile shear zone along which the Jurassic-lower Miocene carbonate sequence of the Pollino unit is strongly deformed.

In this complex geological setting, medium to strong earthquakes ($4 \leq M \leq 6$) occur on the northwest flank of the Pollino Range and Mercure basin area on roughly SE-NW trending normal faults (Brozzetti et al., 2017). The earthquakes accommodate the arc-normal northeast-southwest extension. Left lateral strike-slip regional faults oriented WNW-ESE (Van Dijk et al., 2000) and alignments of East- and West-dipping normal faults have been found in the area. Meanwhile, on the Tyrrhenian coastal side, regional East-dipping normal faults have been recognized across north Calabria.

Figure 1 shows a map of a wide area including the Pollino Range and its surroundings. Here, we show the known faults taken from both the detailed mapping of Brozzetti et al. (2017) for the Pollino range, and ITHACA catalogue for the outermost main structures, as well as other geological features considered in the interpretation. The same figure shows the epicenters of monitored (yellow) and historical (orange) earthquakes occurred in the area (taken from Ferranti et al. (2017)), and the epicentral area of the last seismic sequence (2010 – 2014, red ellipse). The locations of historical earthquakes are achieved using the Boxer method (Gasperini et al., 2010) based on the evaluation of the epicenter as the center of mass of largest intensities. Even if this methodology was tested using more recent epicenters, the uncertainties that afflict these locations are much higher than those of monitored events, in the order of some km. Nevertheless, taken into account the location errors, epicenters follow an SE-to-NW trend through time, at least until the 1998 Mercure basin earthquake.

3. Data and methods

We have analyzed velocity waveforms data recorded by permanent and temporary seismic stations operating in the Pollino area during the 2010 – 2014 seismic sequence. We selected 117 crustal earthquakes of local magnitude (M_L) ranging from 1.8 to 4.3, source-receiver distance between 1 and 72 km, and depths between 2 and 56 km. We performed the waveform selection to obtain a satisfactory coverage of crossing rays across the area. However, while hundreds of events were available in the central part, most of them being located roughly in the same spot, fewer were found in other volumes around the 2010-2014 sequence. Most of the selected events ($\sim$ 80%) are located at depth smaller than 10 km (Supplementary materials, Figure S1). To increase the ray coverage filling gaps were left by shallower we used deeper crustal earthquakes; nevertheless, only 7 of them ($<$ 2%) are deeper than 30 km.

Since the seismic sequence continued for years at a variable rate, the number of temporary stations often changed in the area. The selected data set includes 21 seismic stations, some of which were permanent while others were operated from months to some years by three institutions: 1) *Università della Calabria*; 2) *Istituto Nazionale di Geofisica e Vulcanologia (INGV)*; 3) *GFZ* (Figure 2). Data of INGV and GFZ stations were downloaded from the EIDA online database (Bianchi et al., 2015). The distribution of seismic stations and earthquakes is crucial to test the reliability of our results. Since we used data coming from three different databases, the selected earthquakes were located before any other analysis.

We selected 911 waveforms with clear P-wave phase and coda-to-noise ratio higher than 3 at 30 s from the origin time in the frequency range 1 Hz - 32 Hz. The final dataset also comprises 357 waveforms with clear picking of both P and S waves, the first used for pick-delay mapping. We bandpass-filtered the whole seismograms in 5 frequency bands (1-2 Hz, 2-4 Hz, 4-8 Hz, 8-16 Hz, 16-32 Hz) applying a Butterworth filter of order 4, forward and backwards. We computed envelopes from the absolute value of the Hilbert transform of the signal. We then smoothed them with a moving window of length 8 times the inverse central frequency - an average between what is used between regional (Calvet and Margerin, 2013) and local volcanic (De Siena et al., 2016) scales.

3.1. Peak-delay time measurement and mapping

We measure the peak-delay time as the lag between the P-wave onset and the maximum S wave amplitude (Takahashi et al., 2007). The base-10 logarithm of the peak-delay time ($t_r^T(f)$, in seconds) is related to the base-10 logarithm of the epicentral distance (R, in km) in each frequency band f by:

$$log_{10}(t_r^T(f)) = A_r(f) + B_r(f)log_{10}(R) \quad (1)$$

where A_r and B_r are the coefficients of the fit (Figure S2 in supplementary material). The variations of the peak-delay time with respect to these trends ($\Delta log_{10}(t_r(f))$:

$$\Delta log_{10}(t_r(f) = log_{10}(t_r(f)) - log_{10}(t_r^T(f)) \quad (2)$$

do not depend on geometrical propagation. They are assumed as a measure of the relative strength of accumulated S wave scattering along each ray path (Saito et al., 2002). In other words, high values of $\Delta log_{10}(t_r(f)$ mean that the ray path crosses regions of high heterogeneity (Calvet et al., 2013). For the mapping, we selected the area shown in Figures 1 and 2 (lon: 15.4, 16.4; lat: 39.6, 40.4) and divided it into rectangular blocks of size $0.05° \times 0.05°$. We thus evaluated peak-delays along 2D source-receiver rays and assigned their values to each node with a regionalisation approach (Takahashi et al., 2007) (Figure 4). Even though no exact forward model exists, we tested the stability of the results by repeating the same analysis in a rectangular grid of steps $0.1° \times 0.1°$ (Figure S2). We then interpreted only patterns recovered by the test and where Q_c^{-1} is recovered by resolution tests (see next section).

3.2. Inverse coda-Q measurement and mapping

We consider the energy envelope decay of coda waves described by Aki and Chouet (1975) using the following equation:

$$E(t, f) = S(f)t^{-\alpha}exp\left(\frac{-2\pi ft}{Q_C}\right) \quad (3)$$

where $E(t, f)$ is the power spectral density, $S(f)$ is a source/site term, t is the lapse-time from the origin of the event, and $Q_c^{-1}(f)$ is the frequency-dependent inverse coda quality factor. α is equal to 3/2 in a layer characterized by an anisotropic multiple scattering regime (Paasschens, 1997; Calvet et al., 2013). The choice of the coda window is crucial to map stable lateral variations of seismic attenuation. We want to exclude the increasing transient regime occurring at short lapse time as shown by Calvet and Margerin (2013) while we require a signal-to-noise ratio greater than 5 across the whole window of analysis. Coda windows in our work start at lapse time $t_W = 15s$ from the origin-time of the selected earthquake and are characterized by a length of $L_W = 10s$ (Figure 3). This coda window provides envelopes with sufficient energy for measuring Q_c^{-1} at four of the five previously-mentioned frequency bands (Figure 5). At 18 Hz, a significant number of envelopes present a signal-to-noise ratio lower than 5; we considered the results at this frequency as unreliable and analyzed only the remaining frequencies.

In our time window, equipartition is achieved after 15 seconds (red line in figure 5) while Q_c^{-1} shows no consistent variations with epicentral distance (Supplementary Materials, figure S3). In the absence of leakage (Calvet and Margerin, 2013; Margerin, 2017) we can thus interpret Q_c^{-1} as a measurement of absorption. Still, we need to acknowledge the effect of leakage on our data. Our scale is similar to that of Gaebler et al. (2015) (0.5×0.5 degrees squared), who estimate a transport mean free path of l=50-110 km between 3 and 24 Hz, approximately our frequency range. The ratio between the transport mean free path and the average crustal thickness H=45 km (Piana Agostinetti and Amato, 2009) thus varies between H=0.4 and H=1. The effect of leakage is thus not negligible but still well above the limit (H=0.2) where equipartition brakes down (Margerin, 2017).

We used a non-linear approach to solve equation 3 in the other four frequency bands (1 - 2 Hz, 2 - 4 Hz, 4 - 8 Hz, 8 - 16 Hz). We divided the envelope of seismic coda waves between 15 s and 25 s in windows of length 2s for each source-station pair. Then, we normalized the energy in each smaller window dividing by that of the last window to remove the source effect, $S(f)$. We used a grid search on 1000 trial Q_c values to find the best solution. In each window, we subtracted the normalized energy and the model, then minimized the residual L1 norm for all time windows. This non-linear solution is more stable than the standard linearized technique for coda signals having low signal-to-noise ratios (Ibanez et al., 1993).

We mapped the sensitivity of the Q_c^{-1} parameters to space (x,y) by computing diffusive sensitivity kernels (Del Pezzo et al., 2016) (Figure S4 in Supplementary Material). For each source – receiver pair of coordinates (x_s, y_s) and (x_r, y_r), the kernels are defined as follows:

$$\begin{aligned} f[x,y,x_r,y_r,x_s,y_s] =& \frac{1}{4\pi\delta_x D^2\delta_y} exp\left[-\frac{(x-\frac{x_r+x_s}{2})^2}{2(\delta_x D)^2}+\frac{(y-\frac{y_r+y_s}{2})^2}{0.5(\delta_y D)^2}\right]+ \\ &+\frac{1}{2\pi\delta_x D^2\delta_y} exp\left[-\frac{(x-x_s)^2}{2(\delta_x D)^2}+\frac{(y-y_s)^2}{2(\delta_y D)^2}\right]+ \\ &+\frac{1}{2\pi\delta_x D^2\delta_y} exp\left[-\frac{(x-x_r)^2}{2(\delta_x D)^2}+\frac{(y-y_r)^2}{2(\delta_y D)^2}\right] \end{aligned} \quad (4)$$

where δx and δy are the spatial apertures of the weighting functions along the x and the y axis. These apertures can be set to 0.2 for a wide range of crustal scattering parameters in a diffusive regime (Del Pezzo et al., 2016). We set the same area and grid defined for peak-delay analysis, inverting for the spatial distribution of $Q_c^{-1}(f)$ in space in the four remaining frequency bands (Figure 6). The mapping is performed with the inversion scheme described by De Siena et al. (2017), with the hypothesis that the energy is entirely lost inside the predefined grid. We evaluated effective stability and resolution of the solution by selecting the best damping parameter between the size of the regularized solution and its fit to the given data (L-curves in figure S5). As for peak-delay analysis, we tested the stability of our results with a coarser node spacing (Figure S6). Finally, we tested our resolution performing checkerboard tests with multiple grid node spacing ($0.05° \times 0.05°$ grid in figure S7 and $0.1° \times 0.1°$ grid in figure S8).

3.3. Parameter space variation and mapping

We plotted scattering vs absorption measurements in their parameter space after removing the mean computed over all measurements (De Siena et al., 2016). This graphical method makes results clearer on map, relating the relative variation of $Q_c^{-1}(f)$ (horizontal-axis, absorption) to $\Delta log_{10}(t_r(f)$ (vertical-axis, scattering) and setting a color for each possible combination of the space parameter divided in 4 quadrants (Figure S9). In this case, we set: red for high scattering and high absorption (HS-HA), orange for low scattering and high absorption (LS-HA), light blue for high scattering and low absorption (HS-LA), green for low scattering and low absorption (LS-LA). We additionally set gray for values with a level of discrimination less than 1% of the maximum variations. We characterize each node of the grid with the same palette (Figure 7, left column).

4. Results

Figures 4 and S2 (in Supplementary Materials) show the regionalisation results for peak-delays on 2D map characterized by grids with steps of 0.05° and 0.1°, respectively. Comparison between them shows the stability of patterns of dimension equal or greater than 0.1° × 0.1°. Figures 6 and S6 (in Supplementary Materials) show the $Q_c^{-1}(f)$ results obtained for the same grid steps. At low frequencies, late coda-to-noise ratios are higher thus providing results affected by lower uncertainties. In a given time window, the coda-to-noise ratio progressively decreases as the frequency increases, thus reducing data used for the analysis at higher frequencies and/or reliability of results. For each frequency band, we computed the L curves (log-log plots of the norm of the regularized solution versus the norm of the corresponding residual norm). After testing different damping parameters, we chose 0.1 as the best compromise to obtain scattering and absorption maps at all frequencies.

4.1. Discussion

In Figure 7 we present (left) and interpret (right) the results for each frequency band. Due to the depth of the Moho (Piana Agostinetti and Amato, 2009), we assume that multiple scattering acts in a anisotropic scattering layer. Most earthquakes are located at depths lower than 10 km, supporting this assumption. The effect of leakage may still be important from previous calculations (Margerin, 2017). Still, the Moho in the study area is mostly flat (Piana Agostinetti and Amato, 2009), minimizing the lateral variations produced by this mechanism. In summary, we can safely assume that our results are representative of the shallow crust and look for any relationships between the observed scattering (peak-delay) and absorption (coda-attenuation) patterns and the geological features of the investigated area. We do not observe any orange zone (LS-HA) stable and big enough to be discussed. The Calabro-Lucania coastal range (western side of the maps - Figure 7, left) changes from LS-LA at low frequency (green, 1.5 Hz and 6 Hz) to HS-LA (cyan) at 12 Hz. However, the resolution tests show that the area is unresolved. The same is true for one of the most stable patterns in frequency, i.e., the green LS-LA zone visible in the north-eastern sector of the maps.

A cyan HS-LA pattern both stable in frequency and resolved by our mapping comprises the part of the Lucanian Apennines (named *LA* in Figure 7, right) extending from Mount Sirino to Lake Pertusillo. Geologically, this is a compact carbonate stand-alone block, surrounded by faults and isolated through clay formations. Fractured volumes of minor importance are present in this block due to the high-compression regime in the region. This geological configuration likely explains the high scattering values at all frequencies. The low-absorption values are instead a consequence of the cohesion of the carbonate block, which acts as a shield between the extensive northern hydrocarbon deposit in the Val D'Agri zone and the southern Pollino area.

The red-coloured HS-HA patterns are the most remarkable and well-resolved of our study, and the most interesting for an interpretation in terms of fluid-filled fracture networks (Quintal et al., 2014). The faults located inside it are colored red in the maps on the right side of Figure 7. The Mercure and the Castrovillari basins (MB and CB, respectively) are both characterized by shallow-marine deposits. The former is filled with alluvial, fluvialdeltaic and lacustrine sediments (Ferranti et al., 2017); the latter is filled with clay, sand (in the shallower layer), fine marine sediments, and conglomerates. Both basins are likely characterized by high absorption, contributing to the red pattern. The HS-HA red pattern marks the fault system underneath the Pollino Range at 6 and 12 Hz. We suggest a relationship with the prominent geological characteristic of a multiple fragmented shallow-water carbonate succession. The Lauria mountains (LM) are the north-west extension of the carbonate succession of the Pollino Ridge, and they are characterized by the same HS-HA (red) at the same frequencies.

The HS-HA pattern changes its position with changing frequency. At 1.5 Hz, the red area marks the S-SE sector of the map, crossed by extensive fault networks; at 3 Hz the pattern is still present in the SE sector but becomes predominant in the Pollino area. The red color spreads across the Mercure basins and the Lauria mountains at 6 Hz, and fills the area of the 2010-2014 seismic swarm at 12 Hz. The relatively high-absorption values correlate well with the high v_P/v_S values found in the same area by (Barberi et al., 2004, figure 7) and by Totaro et al. (2015). The results confirm the scenario proposed for the 2010-2014 seismic swarm by Passarelli et al. (2015) of a large role played either by the increase of pore pressure or fluid infiltration within the seismogenic zone in favouring the aseismic slip by lowering the normal stress on the fault plane.

Historical earthquake locations are affected by significant uncertainties, differently from those occurred in the last 20 years. Even considering these uncertainties, the HS-HA pattern migrates with increasing frequency following the chronological order of historical earthquakes from the sixteenth century until Pollino swarm. The most recent earthquakes, e.g., the Mercure basin earthquake and the Pollino swarm itself, likely reactivate small fracture networks as fluids migrate along the main faults, modifying the way fluids permeate fault structures. Poro-elasticity studies proved the central role of fluid pressure diffusion between connected fractures, and showed how the behavior of the connected fracture system is frequency dependent (Quintal et al., 2014).

Hunziker et al. (2018) pointed out that the still-unknown relationship between seismic attenuation, diffusion of fluid pressure and fracture connectivity can be crucial to identify a highly-fractured volume and track its hydraulic behavior. Our results strongly suggest such a relationship in some of the fault areas. Changes of peak-delay and Q_c^{-1} with frequency mark in fact heterogeneity of different size (Saito et al., 2002): in the case of faults, small fractured volumes in active zones can only be imaged by shorter-wavelength (higher-frequency) attenuation parameters. While these fracture networks heal quickly, in seismically-active areas they continuously reactivate due to distant seismicity (Xue et al., 2009), at least where fluids are abundant. The healing of smaller fractures is instead permanent in areas not deformed by recent activity. Here, larger unhealed structures should be visible from their long-wavelength (low-frequency) high-scattering and high-absorption signatures. We thus infer that the migration of the HS-HA patterns with increasing frequency shows the effect of fracture healing (Xue et al., 2009).

The anomalies effectively track the migration of seismogenic zones since the sixteenth century (Figure 1) by mapping scattering and absorption changes in frequency inside the fracture-network. While we already confirmed the role of fluids in nucleating historical and recent seismicity (Passarelli et al., 2015), our results support the view that the Pollino swarm represents a change in the usual seismicity trend of the area. The stop to the SE-to-NW migration of the HS-HA pattern at 12 Hz is, in our interpretation, due to the barrier represented by the high-scattering compressed carbonates under the Lucanian Apennines. Since the Pollino swarm, a permanent network has been installed in the area and may provide sufficient data to test our inferences in the presence of renewed seismic activity.

5. Conclusions

Peak-delay and inverse coda quality factor have been measured together and mapped using a 2D approximation in four frequency bands to image the scattering attenuation and absorption properties of the slowly-deforming Pollino area (Southern Italy). The pattern of anomalies obtained from our analysis shows a correlation with the geological features of the area and with the progressive shift in location of earthquakes. High-scattering and high-absorption anomalies (HS-HA) change their position from inactive faults in the south/southeastern Castrovillari basin (1.5 Hz) to the northwestern Mercure Basin and Pollino swarm area (6-12 Hz) across the fault systems (3 Hz). We infer that the Lucanian Apennine compressed carbonates, marked by high-scattering, constitute a barrier for fracture network connectivity and fluid propagation. The two sedimentary basins are characterized by high absorption. However, high-absorption and high-scattering patterns observed at higher frequency likely reveal fluid-filled fractured volumes of shorter dimension.

At low frequency, the patterns map the structures of the fault systems inactive (1.5 Hz) or fractured by seismic sequences dating back to the sixteenth-eighteenth century (3 Hz). Here, shorter fractures are progressively healed, with high scattering and absorption marking extended fault areas permanently deformed. At 6 Hz the anomalies characterize the NW branch of the faults, tracking the seismic activity of the last two centuries up to the Mercure basin earthquake (1998). The earthquake migration is likely due to the progressive increase of the contribution of small-scale fluid-filled fractures to scattering and absorption. At the highest frequency (12 Hz) the HS-HA area becomes broader and covers the fault system that generated the last Pollino swarm (2010-2014), SW of the Mercure basin. We infer that the fracture propagation trend was blocked NW by the high-scattering Lucanian Apennine carbonates. The scattering and absorption picture described by our interpretation provides an independent view on the well-known geological features of the area, the known fault network, and the migration of seismogenic zones through the last five centuries, focusing on the important role of fluid saturation. Further observations with better distributed earthquakes and seismic stations may give deeper insight into the physics underlying these processes. More efforts are necessary to apply successfully the laboratory results to the Earth crust, that means in our case to measure or estimate the time scale of processes such as fracture healing and fluid migration throughout connected / not connected fracture networks. Still, our work supports the view that attenuation and scattering parameters are able to reconstruct shape and dynamics of fluid-filled fracture networks in fault areas.

6. Acknowledgements

We thank Giuseppe Palladino and professor Robert Butler for sharing their expertise about the geological features of the target area and Roberto Emanuele Rizzo for the relevant suggestions about the dynamics of fluids through fractures. Incisive comments from two anonymous reviewers greatly improved the quality of the paper. The program used to compute the analysis is the MATLAB® code $MuRAT5.3.6.m$, available for downloading at: *https://github.com/ferdinandonapolitano/Attenuation*.
The ITHACA catalogue we use can be found at:
http://www.isprambiente.gov.it/it/progetti/suolo-e-territorio-1/ithaca-catalogo-delle-faglie-capaci.

Aki, K., Chouet, B., 1975. Origin of coda waves: Source, attenuation, and scattering effects. Journal of Geophysical Research 80 (23), 3322–3342. URL `http://doi.wiley.com/10.1029/JB080i023p03322`

Amoroso, O., Russo, G., De Landro, G., Zollo, A., Garambois, S., Mazzoli, S., Parente, M., Virieux, J., 2017. From velocity and attenuation tomography to rock physical modeling: Inferences on fluid-driven earthquake processes at the Irpinia fault system in southern Italy. Geophysical Research Letters 44 (13), 6752–6760.
URL `https://agupubs.onlinelibrary.wiley.com/doi/abs/10.1002/2016GL072346`

Barberi, G., Cosentino, M. T., Gervasi, A., Guerra, I., Neri, G., Orecchio, B., 2004. Crustal seismic tomography in the Calabrian Arc region, south Italy. Physics of the Earth and Planetary Interiors 147 (4), 297–314.

Bianchi, M., Evans, P. L., Heinloo, A., Quinteros, J., 2015. WebDC3 Web Interface.
URL http://geofon.gfz-potsdam.de/software/webdc3

Borleanu, F., De Siena, L., Thomas, C., Popa, M., Radulian, M., 2017. Seismic scattering and absorption mapping from intermediate-depth earthquakes reveals complex tectonic interactions acting in the Vrancea region and surroundings (Romania). Tectonophysics 706-707, 129–142.
URL http://www.sciencedirect.com/science/article/pii/S0040195117301476

Brozzetti, F., Cirillo, D., de Nardis, R., Cardinali, M., Lavecchia, G., Orecchio, B., Presti, D., Totaro, C., 2017. Newly identified active faults in the Pollino seismic gap, southern Italy, and their seismotectonic significance. Journal of Structural Geology 94, 13–31.
URL http://dx.doi.org/10.1016/j.jsg.2016.10.005

Calvet, M., Margerin, L., 2013. Lapse-time dependence of coda Q: Anisotropic multiple-scattering models and application to the Pyrenees. Bulletin of the Seismological Society of America 103 (3), 1993–2010.

Calvet, M., Sylvander, M., Margerin, L., Villaseñor, A., 2013. Spatial variations of seismic attenuation and heterogeneity in the Pyrenees: Coda Q and peak delay time analysis. Tectonophysics 608, 428–439.
URL http://dx.doi.org/10.1016/j.tecto.2013.08.045

Cello, G., Invernizzi, C., Mazzoli, S., 1996. Structural signature of tectonic processes in the Calabrian Arc, southern Italy: Evidence from the

oceanic-derived Diamante-Terranova unit. Tectonics 15 (1), 187–200.
URL https://agupubs.onlinelibrary.wiley.com/doi/abs/10.1029/95TC02356

Cheloni, D., D'Agostino, N., Selvaggi, G., Avallone, A., Fornaro, G., Giuliani, R., Reale, D., Sansosti, E., Tizzani, P., 2017. Aseismic transient during the 2010-2014 seismic swarm: Evidence for longer recurrence of M $\geq$ 6.5 earthquakes in the Pollino gap (Southern Italy)? Scientific Reports 7 (1), 1–10.

Cinti, F. R., Cucci, L., Pantosti, D., D'Addezio, G., Meghraoui, M., 1997. A major seismogenic fault in a 'silent area': the Castrovillari fault (southern Apennines, Italy). Geophysical Journal International 130, 595–605.

Cinti, F. R., Moro, M., Pantosti, D., Cucci, L., D'Addenzio, G., 2002. New constraints on the seismic history of the Castrovillari fault in the Pollino gap (Calabria, southern Italy). Journal of Seismology 6, 199—-217.

De Siena, L., Amoruso, A., Del Pezzo, E., Wakeford, Z., Castellano, M., Crescentini, L., 2017. Space-weighted seismic attenuation mapping of the aseismic source of Campi Flegrei 1983–1984 unrest. Geophysical Research Letters 44 (4), 1740–1748.

De Siena, L., Calvet, M., Watson, K. J., Jonkers, A. R. T., Thomas, C., 2016. Seismic scattering and absorption mapping of debris flows, feeding paths, and tectonic units at Mount St. Helens volcano. Earth and Planetary Science Letters 442, 21–31.
URL http://dx.doi.org/10.1016/j.epsl.2016.02.026

De Siena, L., Del Pezzo, E., Thomas, C., Curtis, A., Margerin, L., 2013. Seismic energy envelopes in volcanic media: In need of boundary conditions. Geophysical Journal International 195 (2), 1102–1119.

Del Pezzo, E., Ibañez, J., Prudencio, J., Bianco, F., De Siena, L., 2016. Absorption and scattering 2-D volcano images from numerically calculated space-weighting functions. Geophysical Journal International 206 (2), 742–756.

Faccenna, C., Davy, P., Brun, J.-P., Funiciello, R., Giardini, D., Mattei, M., Nalpas, T., 1996. The dynamics of back-arc extension: an experimental approach to the opening of the Tyrrhenian Sea. Geophysical Journal International 126 (3), 781–795.
URL https://onlinelibrary.wiley.com/doi/abs/10.1111/j.1365-246X.1996.tb04702.x

Ferranti, L., Milano, G., Pierro, M., 2017. Insights on the seismotectonics of the western part of northern Calabria (southern Italy) by integrated geological and geophysical data: Coexistence of shallow extensional and deep strike-slip kinematics. Tectonophysics 721 (October), 372–386.
URL http://dx.doi.org/10.1016/j.tecto.2017.09.020

Gaebler, P. J., Eulenfeld, T., Wegler, U., 2015. Seismic scattering and absorption parameters in the W-Bohemia / Vogtland region from elastic and acoustic radiative transfer theory, 1471–1481.

Gasperini, P., Vannucci, G., Tripone, D., Boschi, E., 2010. The Location and Sizing of Historical Earthquakes Using the Attenuation of Macroseismic Intensity with Distance 100 (5), 2035–2066.

Guerra, I., Harabaglia, P., Gervasi, A., Rosa, A. B., dec 2005. The 1998-1999 Pollino (Southern Apennines, Italy) seismic crisis: tomography of a sequence. Annals of Geophysics 48 (6).
URL https://www.annalsofgeophysics.eu/index.php/annals/article/view/3249

Gusev, A. A., Abubakirov, I. R., 1999. Vertical profile of effective turbidity reconstructed from broadening of incoherent body-wave pulses — I . General approach and the inversion procedure. Geophys. J. Int. 136, 295–308.

Hennino, R., Trégourès, N., Shapiro, N. M., Margerin, L., Campillo, M., van Tiggelen, B. A., Weaver, R. L., 2001. Observation of equipartition of seismic waves. Physical Review Letters 86 (15), 3447–3450.

Hunziker, J., Favino, M., Caspari, E., Quintal, B., Rubino, J. G., Krause, R., Holliger, K., 2018. Seismic Attenuation and Stiffness Modulus Dispersion in Porous Rocks Containing Stochastic Fracture Networks. Journal of Geophysical Research: Solid Earth 123 (1), 125–143.
URL https://agupubs.onlinelibrary.wiley.com/doi/abs/10.1002/2017JB014566

Ibanez, J. M., Del Pezzo, E., Martini, M., Patanè, D., de Miguel, F., Vidal, F., Morales, J., 1993. Estimates of Coda-Q Using a Non-Linear Regression. J. Phys. Earth 41, 203–219.

Landgraf, A., Kübler, S., Hintersberger, E., Stein, S., 2017. Active tectonics, earthquakes and palaeoseismicity in slowly deforming continents. Geological Society, London, Special Publications 432 (1), 1–12.
URL https://pubs.geoscienceworld.org/books/book/1937/chapter/107685676/

Lohman, R. B., McGuire, J. J., 2007. Earthquake swarms driven by aseismic creep in the Salton Trough, California. Journal of Geophysical Research: Solid Earth 112 (4), 1–10.

Margerin, L., 2017. Breakdown of equipartition in diffuse fields caused by energy leakage. European Physical Journal: Special Topics 226 (7), 1353–1370.

Margerin, L., Planès, T., Mayor, J., Calvet, M., 2015. Sensitivity kernels for coda-wave interferometry and scattering tomography: Theory and numerical evaluation in two-dimensional anisotropically scattering media. Geophysical Journal International 204 (1), 650–666.

Margheriti, L., Amato, A., Braun, T., Cecere, G., D'Ambrosio, C., De Gori, P., Delladio, A., Gervasi, A., Govoni, A., Guerra, I., Lucente, F. P., Moretti, M., Selvaggi, G., 2013. Emergenza nell'area del Pollino: le attività della rete sismica mobile. Tech. rep.

Mayor, J., Calvet, M., Margerin, L., Vanderhaeghe, O., Traversa, P., 2016. Crustal structure of the Alps as seen by attenuation tomography. Earth and Planetary Science Letters 439, 71–80.
URL http://dx.doi.org/10.1016/j.epsl.2016.01.025

Napolitano, F., Gervasi, A., La Rocca, M., Guerra, I., Scarpa, R., 2018. Site effects in the pollino region from the HVSR and polarization of seismic noise and earthquakes. Bulletin of the Seismological Society of America 108 (1), 309–321.

Obermann, A., Planès, T., Larose, E., Campillo, M., 2013. Imaging preeruptive and coeruptive structural and mechanical changes of a volcano with ambient seismic noise. Journal of Geophysical Research: Solid Earth 118 (12), 6285–6294.

Paasschens, J., 1997. Solution of the time-dependent Boltzmann equation. Physical Review E 56 (1), 1135–1141.

Passarelli, L., Hainzl, S., Cesca, S., Maccaferri, F., Mucciarelli, M., Roessler, D., Corbi, F., Dahm, T., Rivalta, E., 2015. Aseismic transient driving the swarm-like seismic sequence in the Pollino range, Southern Italy. Geophysical Journal International 201 (3), 1553–1567.

Passarelli, L., Roessler, D., Aladino, G., Maccaferri, F., Moretti, M., Lucente;, F. P., Braun, T., De Gori, P., Margheriti, L., Woith, H., Sebastian, H., Eleonora, R., Dahm, T., 2012. Pollino Seismic Experiment (2012-2014). Deutsches GeoForschungsZentrum GFZ Other/Seis.

Peng, Z., Gomberg, J., 2010. An integrated perspective of the continuum between earthquakes and slow-slip phenomena. Nature Geoscience 3 (9), 599–607.
URL http://dx.doi.org/10.1038/ngeo940

Piana Agostinetti, N., Amato, A., 2009. Moho depth and Vp/Vs ratio in peninsular Italy from teleseismic receiver functions. Journal of Geophysical Research 114 (B6), B06303.
URL http://doi.wiley.com/10.1029/2008JB005899

Quintal, B., Jänicke, R., Rubino, J. G., Steeb, H., Holliger, K., 2014. Sensitivity of S-wave attenuation to the connectivity of fractures in fluid-saturated rocks. Geophysics 79 (5), WB15–WB24.
URL http://library.seg.org/doi/10.1190/geo2013-0409.1

Rovida, A., Camassi, R., Gasperini, P., Stucchi, M., 2011. CPTI11, the 2011 version of the Parametric Catalogue of Italian Earthquakes.
URL http://emidius.mi.ingv.it/CPTI, DOI: 10.6092/INGV.IT-CPTI11

Saito, T., Sato, H., Ohtake, M., 2002. Envelope broadening of spherically outgoing waves in three-dimensional random media having power law spectra. Journal of Geophysical Research 107.

Sato, H., Fehler, M. C., Maeda, T., 2012. SeismicWave Propagation and Scattering in the Heterogeneous Earth: Second Edition. Springer, New York, USA.

Scionti, V., Galli, P., Chiodo, G., 2006. The Calabrian seismicity during the Viceroyalty of Naples: Sources silence or silent sources? the case of the strong 1744 earthquake. Bollettino di Geofisica Teorica ed Applicata 47 (1-2), 53–72.

Shapiro, N. M., Campillo, M., Margerin, L., Singh, S. K., Kostoglodov, V., Pacheco, J., 2000. The energy partitioning and the diffusive character of the seismic coda. Bulletin of the Seismological Society of America 90 (3), 655–665.

Souriau, A., Chaljub, E., Cornou, C., Margerin, L., Calvet, M., Maury, J., Wathelet, M., Grimaud, F., Ponsolles, C., Pequegnat, C., Langlais, M., Guéguen, P., 2011. Multimethod characterization of the French-Pyrenean valley of bagnères-de-bigorre for seismic-hazard evaluation: Observations and models. Bulletin of the Seismological Society of America 101 (4), 1912–1937.

Takahashi, T., Sato, H., Nishimura, T., Obara, K., 2007. Strong inhomogeneity beneath quaternary volcanoes revealed from the peak delay analysis of S-wave seismograms of microearthquakes in northeastern Japan. Geophysical Journal International 168 (1), 90–99.

Tertulliani, A., Cucci, L., 2014. New Insights on the Strongest Historical Earthquake in the Pollino Region (Southern Italy). Seismological Research Letters 85 (3), 743–751.
URL http://srl.geoscienceworld.org/cgi/doi/10.1785/0220130217

Totaro, C., Seeber, L., Waldhauser, F., Steckler, M., Gervasi, A., Guerra, I., Orecchio, B., Presti, D., 2015. An intense earthquake swarm in the southernmost apennines: Fault architecture from high-resolution hypocenters and focal mechanisms. Bulletin of the Seismological Society of America 105 (6), 3121–3128.

Ugalde, A., Vargas, C., Pujades, L., Canas, J., 2002. Seismic coda attenuation after the Mw= 6.2 Armenia (Colombia) earthquake of 25 January 1999. Journal of Geophysical Research: Solid Earth 107 (6).

Van Dijk, J. P., Bello, M., Brancaleoni, G. P., Cantarella, G., Costa, V., Frixa, A., Golfetto, F., Merlini, S., Riva, M., Torricelli, S., Toscano, C., Zerilli, A., 2000. A regional structural model for the northern sector of the Calabrian Arc (southern Italy). Tectonophysics 324 (4), 267–320.

Xue, H., Ogawa, K., Shoji, T., 2009. Effect of welded mechanical heterogeneity on local stress and strain ahead of stationary and growing crack tips. Nuclear Engineering and Design 239 (4), 628–640.
URL `http://www.sciencedirect.com/science/article/pii/S0029549309000314`

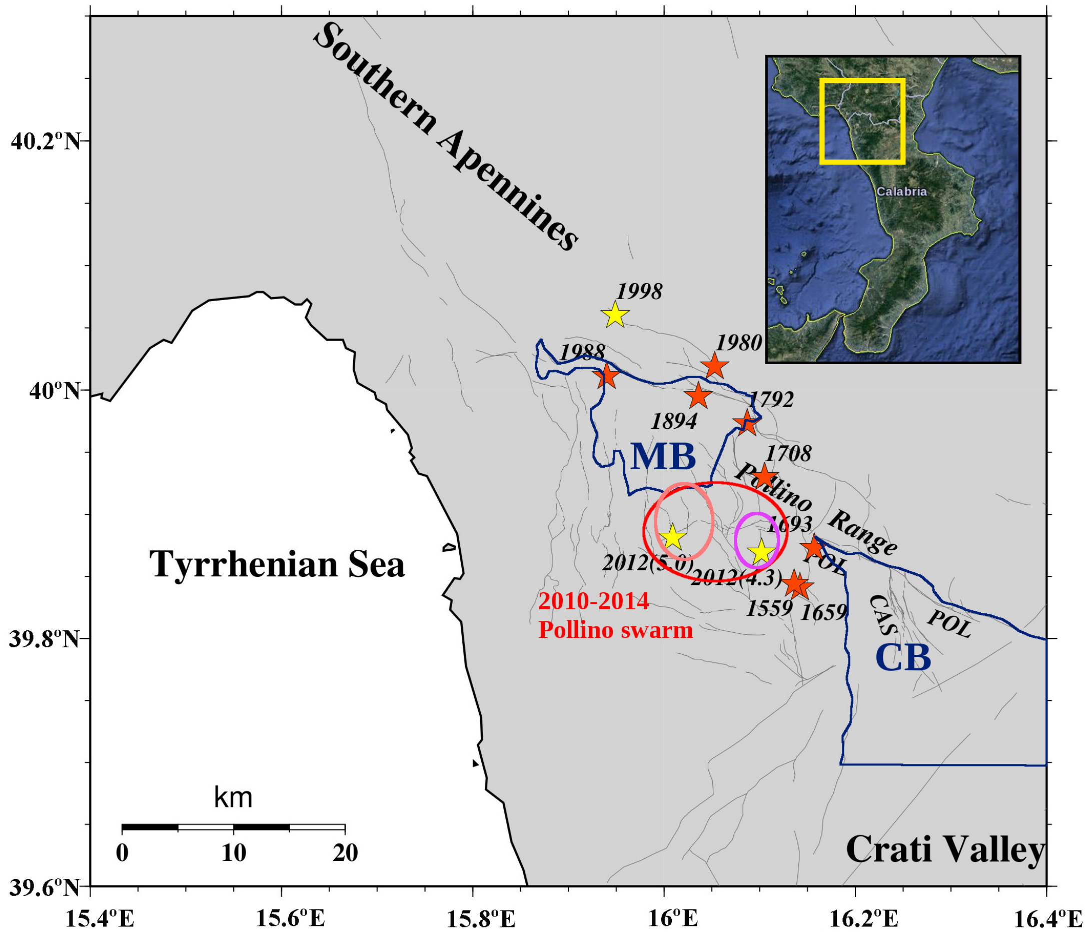

Figure 1: Map of the Pollino transition zone, located between the southern Apennines and the Crati Valley (yellow rectangle in the top right panel). Orange stars represent the presumed epicenters of historical earthquakes until 1988, yellow stars represent mainshocks occurred in the area in the last 20 years. MB and CB, bordered by blue lines, are the Mercure Basin and the castrovillari Basin, respectively. CAS and POL show the Castrovillari and Pollino Faults. The red ellipse surrounds the area of the 2010-2014 seismic swarm, which occurred in two slightly separated areas (smaller ellipses). Thin grey lines are the detailed faults from Brozzetti et al. (2017) in the Pollino area and from ITHACA catalogue for the outermost faults surrounding the Pollino area.

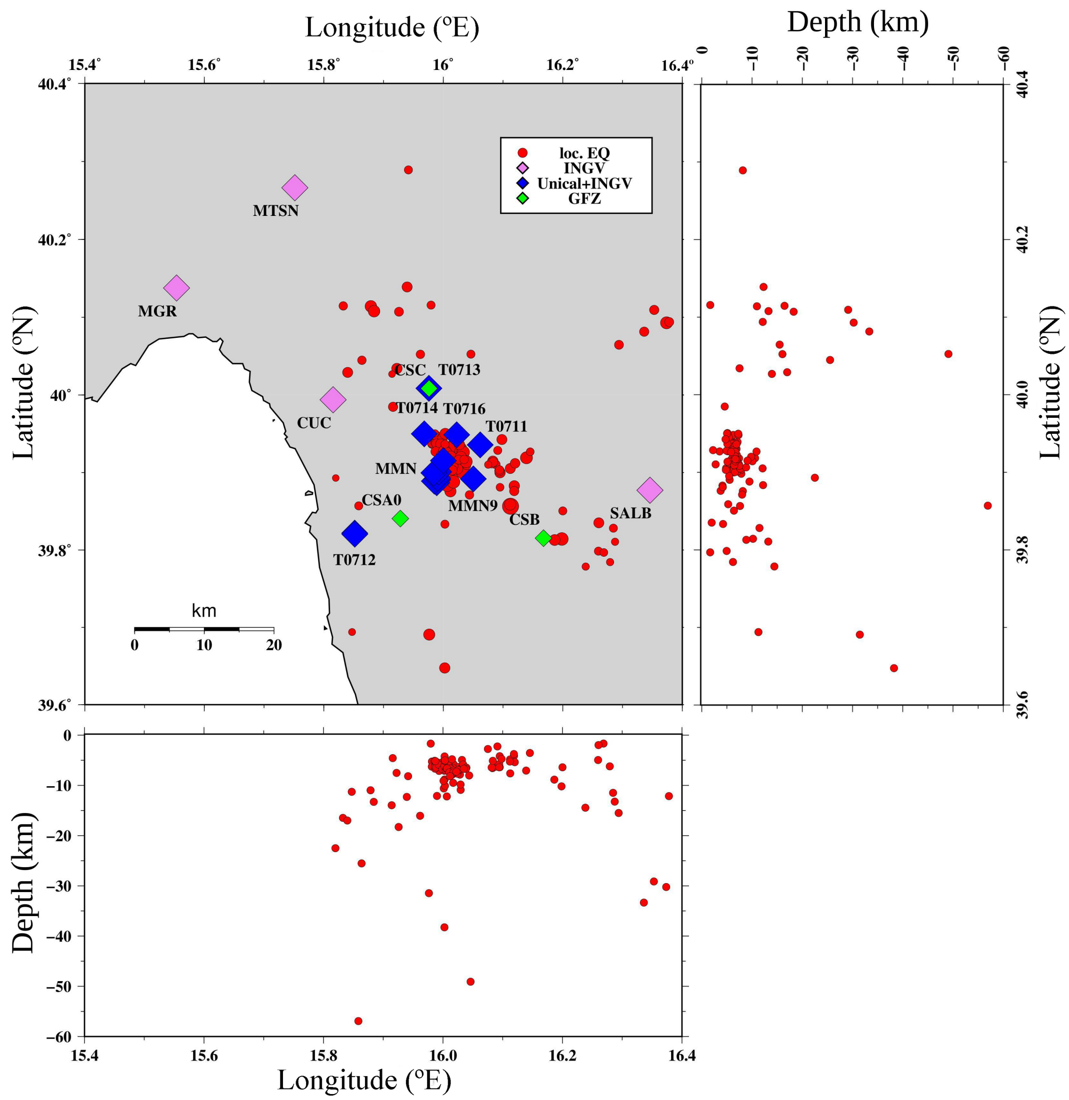

Figure 2: Map of the study area showing earthquakes used in this work (red circles) and seismic stations divided in three groups: permanent and temporary stations operated by the *Istituto Nazionale di Geofisica e Vulcanologia, INGV* (blue, Margheriti et al., 2013); temporary stations installed by GFZ (green, FDSN network code 4A, (Passarelli et al., 2012)); permanent and temporary stations operated by *Università della Calabria* (blue).

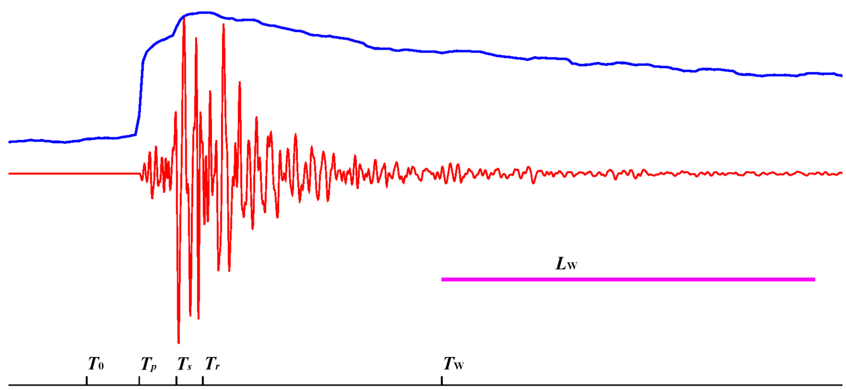

Figure 3: Example of a waveform (red line) used in this work and its envelope (blue line). T_p and T_s the P- and S-wave arrivals, T_r is the time at which the waveform reaches the maximum value, T_W is the beginning of the analysis window and L_W is its length. All these times are referenced to the origin time T_0.

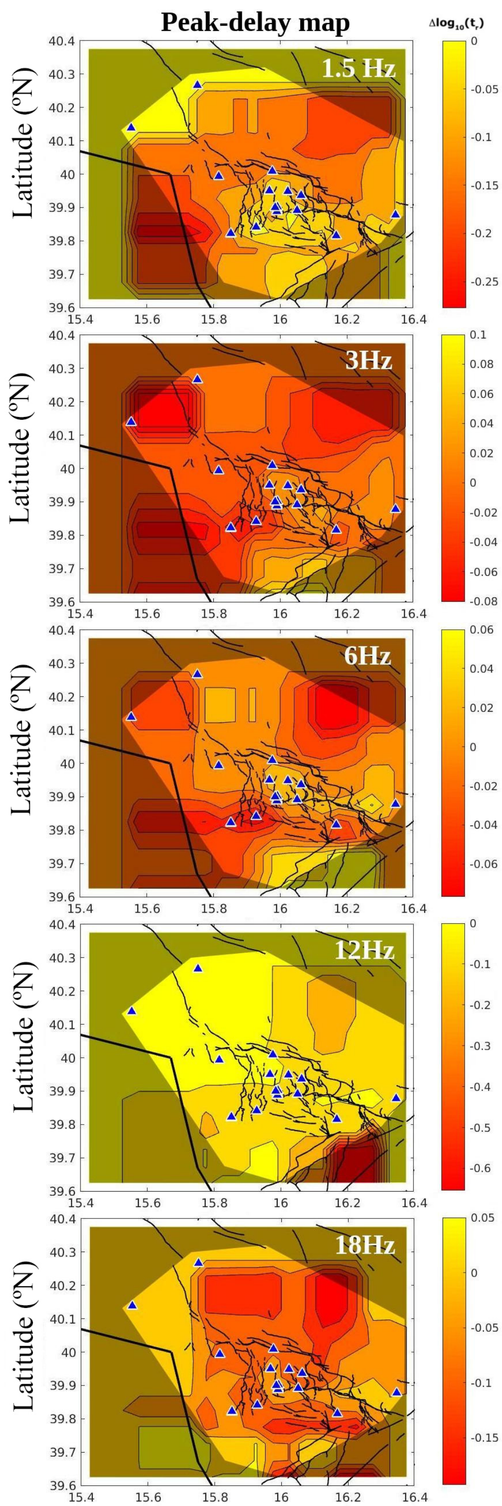

Figure 4: Peak-delay map. Central frequency is shown on the top-right for each panel, blue triangles represent seismic stations used in this work. Yellow colors represent high-scattering zones, red colors represent low-scattering zones.

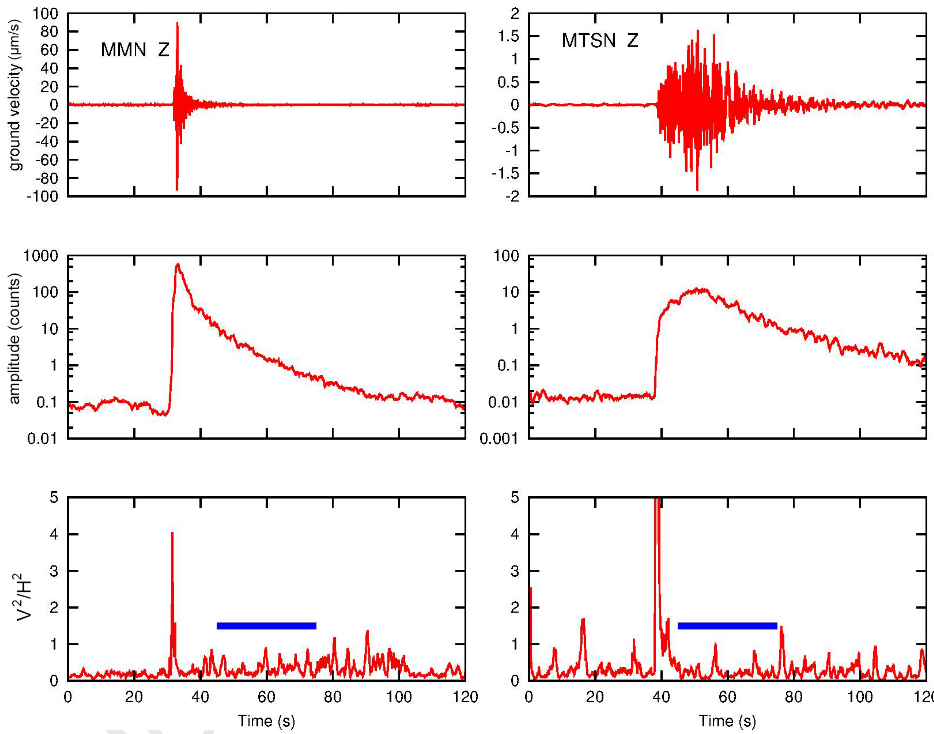

Figure 5: Equipartition of energy shown for one two earthquakes. The two earthquakes are characterized by small (4 km, on the left) and long (44 km, on the right) epicentral distance. From top to bottom: chosen seismograms; plot of the smoothed envelope and the mean noise amplitude; ratio between the kinetic energy of the vertical and horizontal components, V^2/H^2. Blue segments represent the windows chosen to compute coda analysis.

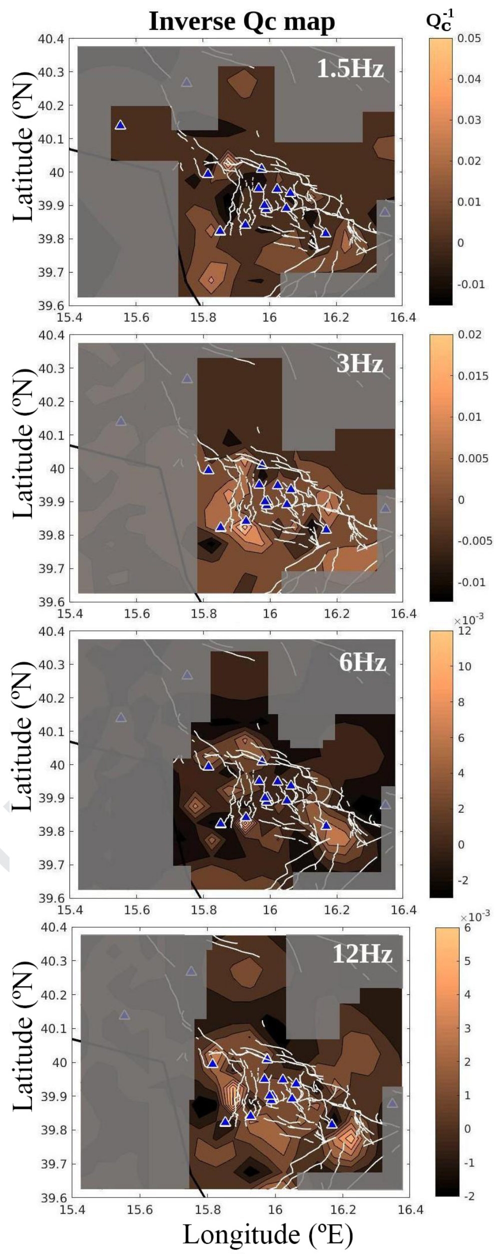

Figure 6: Inverse Q_C map. Central frequency is shown on the top-right for each panel, blue triangles represent seismic stations used in this work.

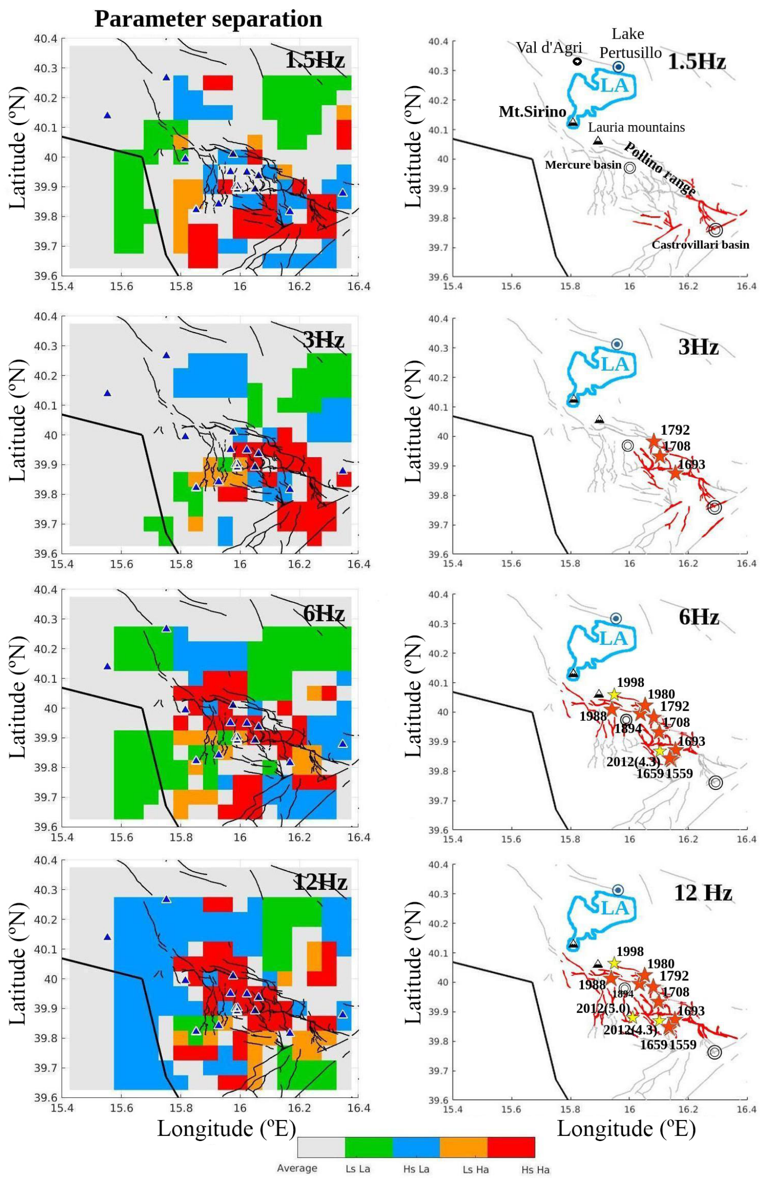

Figure 7: Attenuation and scattering results (left) and schematic interpretation of the stable and resolved patterns (right) obtained in 4 frequency ranges. Palette used: red - high scattering/high absorption, orange - low scattering/high absorption, cyan - high scattering/low absorption and green - low scattering/low absorption. Blue triangles show the seismic stations. The cyan pattern corresponding to the Lucanian Apennines (shortly named *LA*) extends from the Mount Sirino (SW) to the Lake Pertusillo (NE). Faults are coloured and stars (orange for earthquakes before 1998, yellow for more recent earthquakes) are displayed each time they are located in a red high scattering/high absorption block.

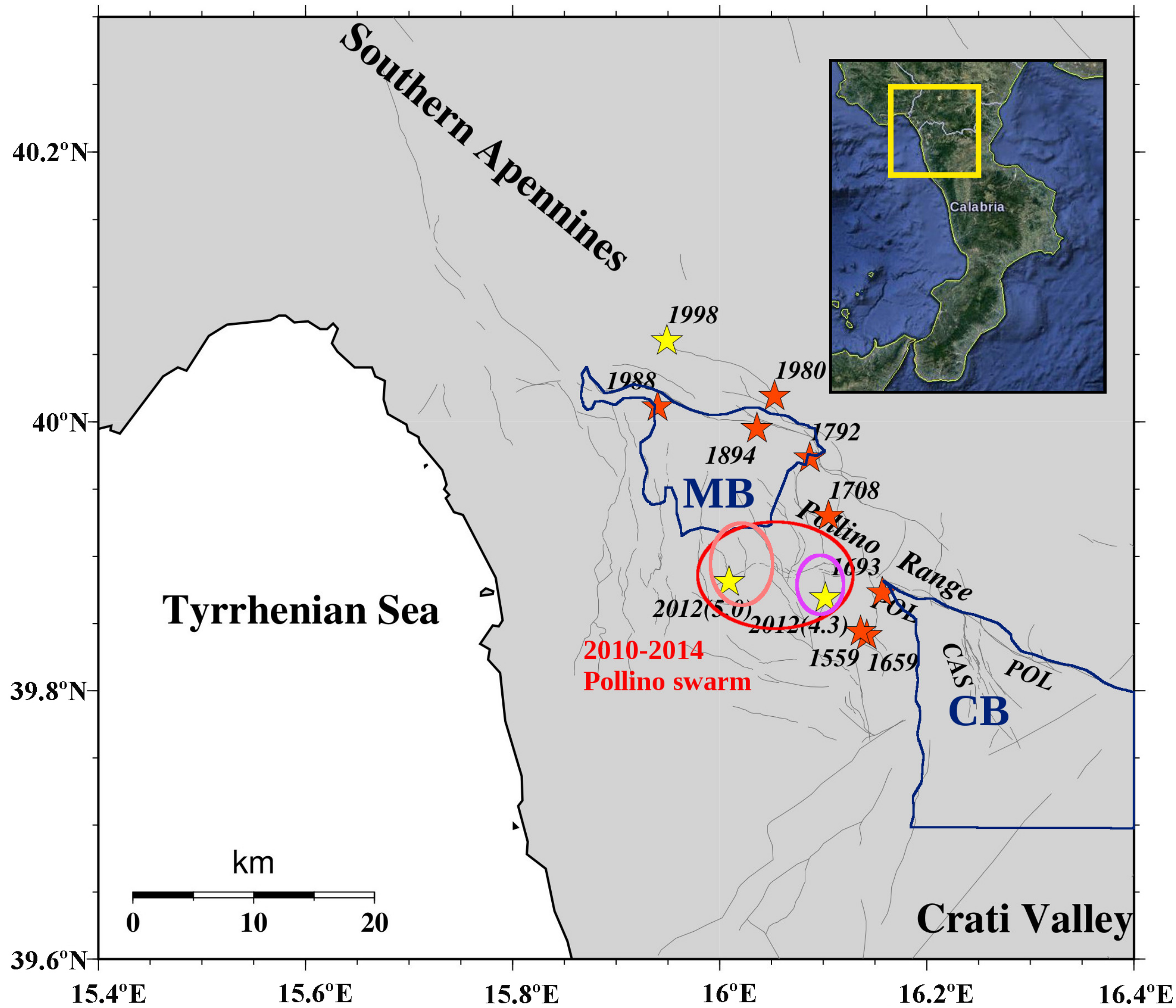
Southern Apennines
40.2°N
40°N
39.8°N
39.6°N
15.4°E
15.6°E
15.8°E
16°E
16.2°E
16.4°E
Calabria
1998
1988
1980
1894
1792
1708
MB
Pollino
Range
1693
POL
2012(5.0)
2012(4.3)
1559
1659
CAS
POL
CB
2010-2014
Pollino swarm
Tyrrhenian Sea
km
0
10
20
Crati Valley

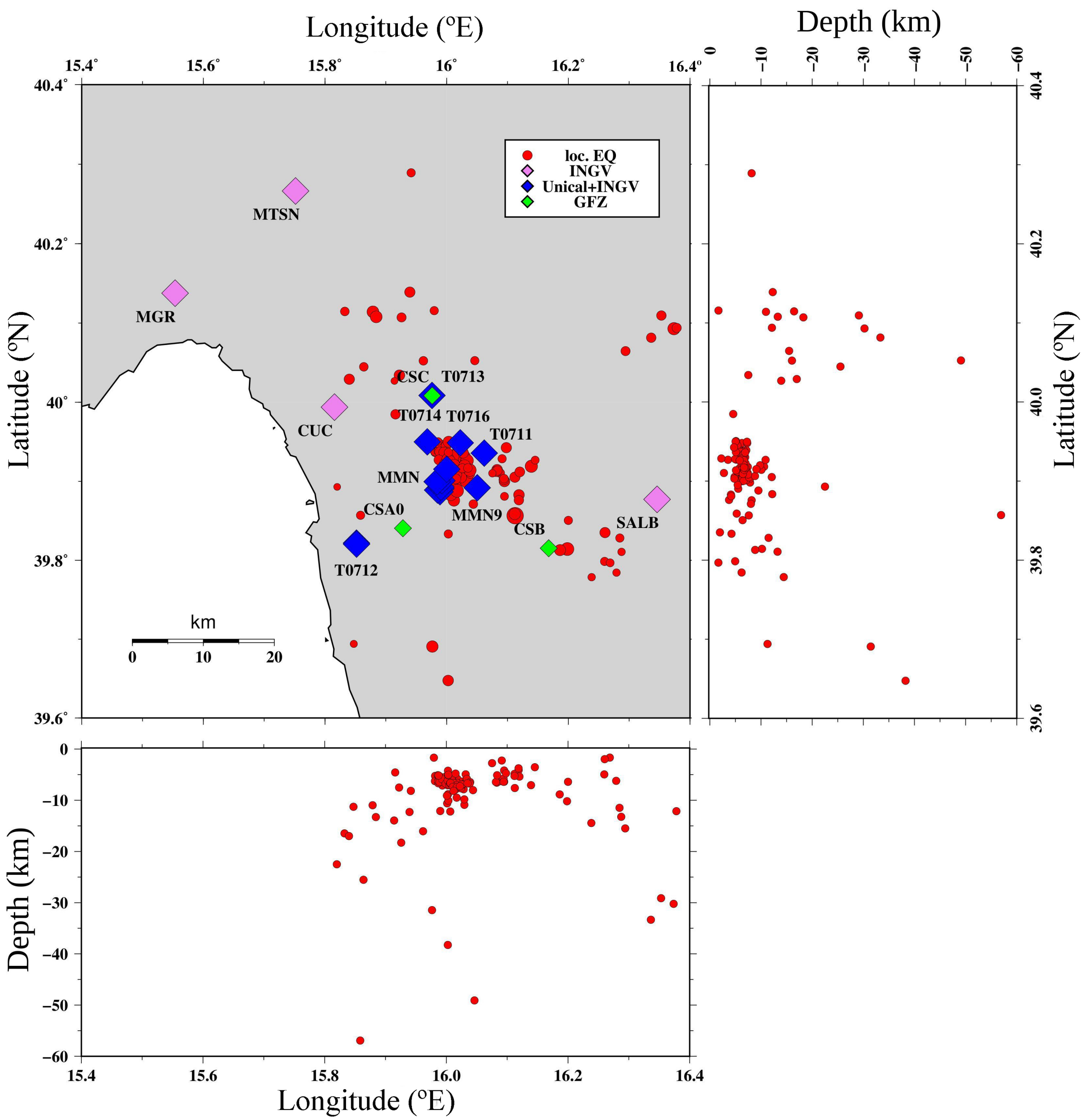
Longitude (°E)
15.4° 15.6° 15.8° 16° 16.2° 16.4°
40.4° 40.2° 40° 39.8° 39.6°
Latitude (°N)
Depth (km)
0 −10 −20 −30 −40 −50 −60
40.4 40.2 40.0 39.8 39.6
Latitude (°N)
loc. EQ
INGV
Unical+INGV
GFZ
MTSN
MGR
CSC
T0713
CUC
T0714
T0716
T0711
MMN
CSA0
MMN9
CSB
SALB
T0712
km
0 10 20
Depth (km)
0 −10 −20 −30 −40 −50 −60
15.4 15.6 15.8 16.0 16.2 16.4
Longitude (°E)

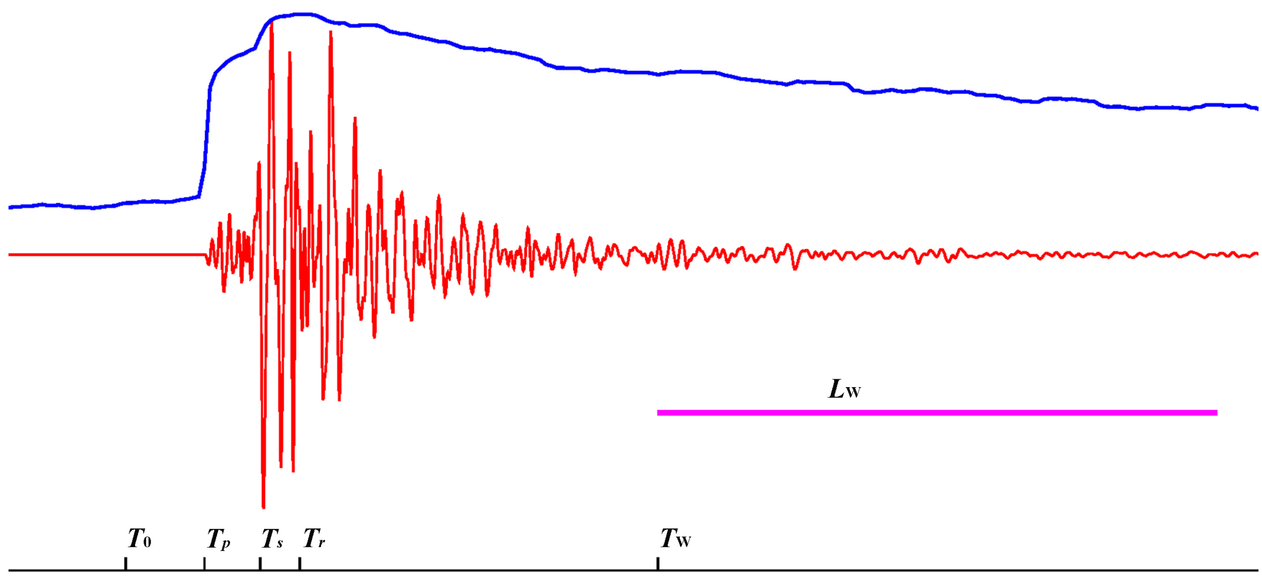

Lw
T0
Tp
Ts
Tr
Tw

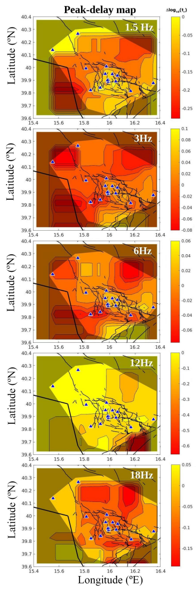
Peak-delay map
Δlog₁₀(tᵣ)
1.5 Hz
3Hz
6Hz
12Hz
18Hz
Latitude (ºN)
Longitude (ºE)

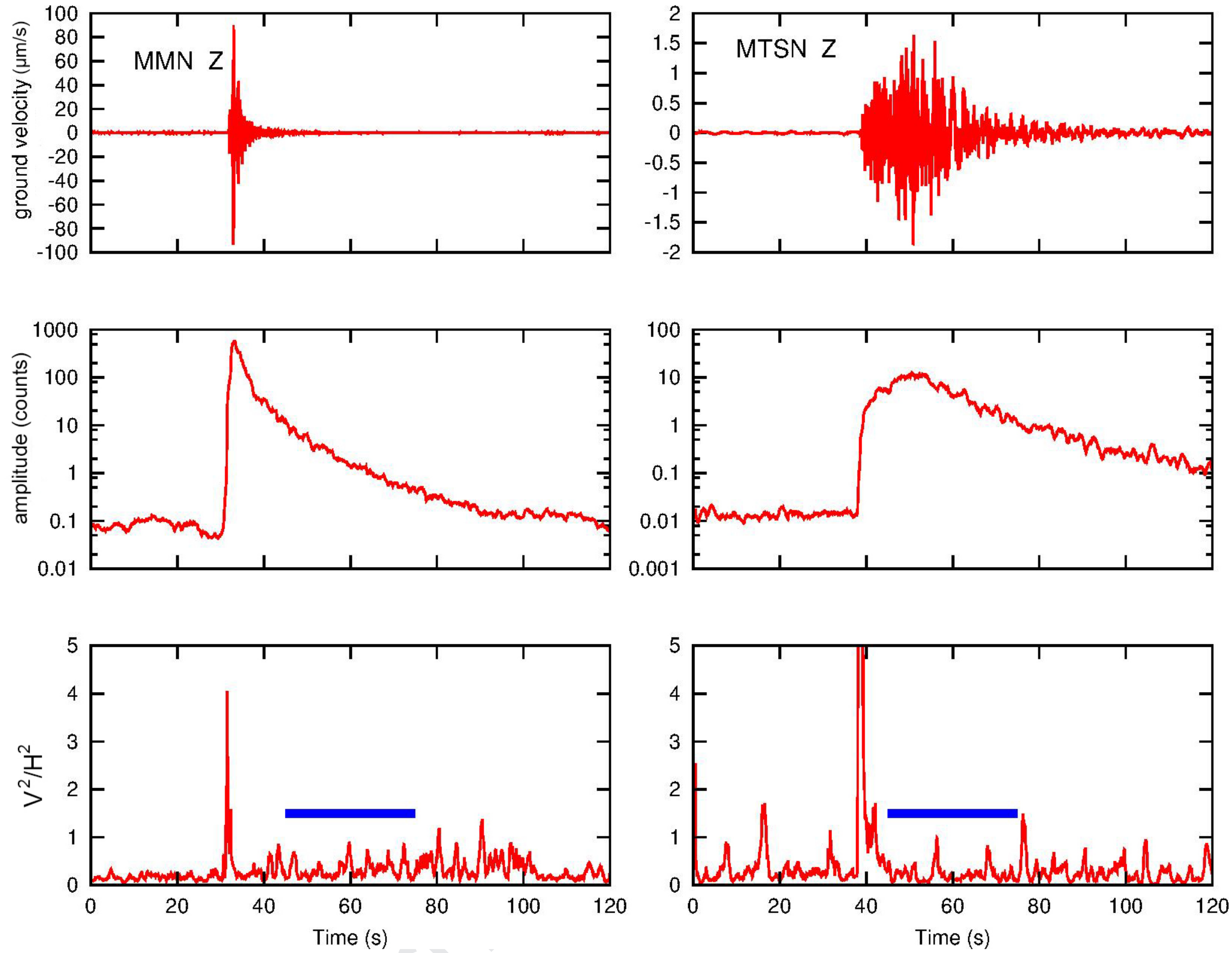
MMN Z
MTSN Z
ground velocity (µm/s)
amplitude (counts)
V2/H2
Time (s)
Time (s)

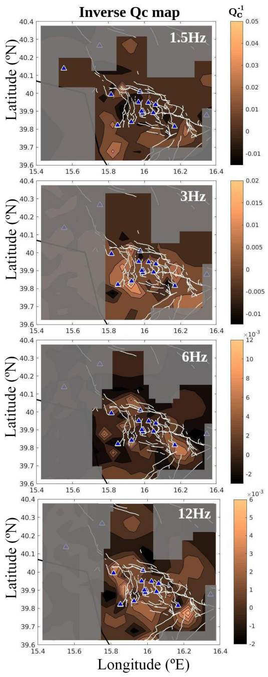
Inverse Qc map
Q_C^{-1}
1.5Hz
3Hz
6Hz
12Hz
Latitude (ºN)
Longitude (ºE)

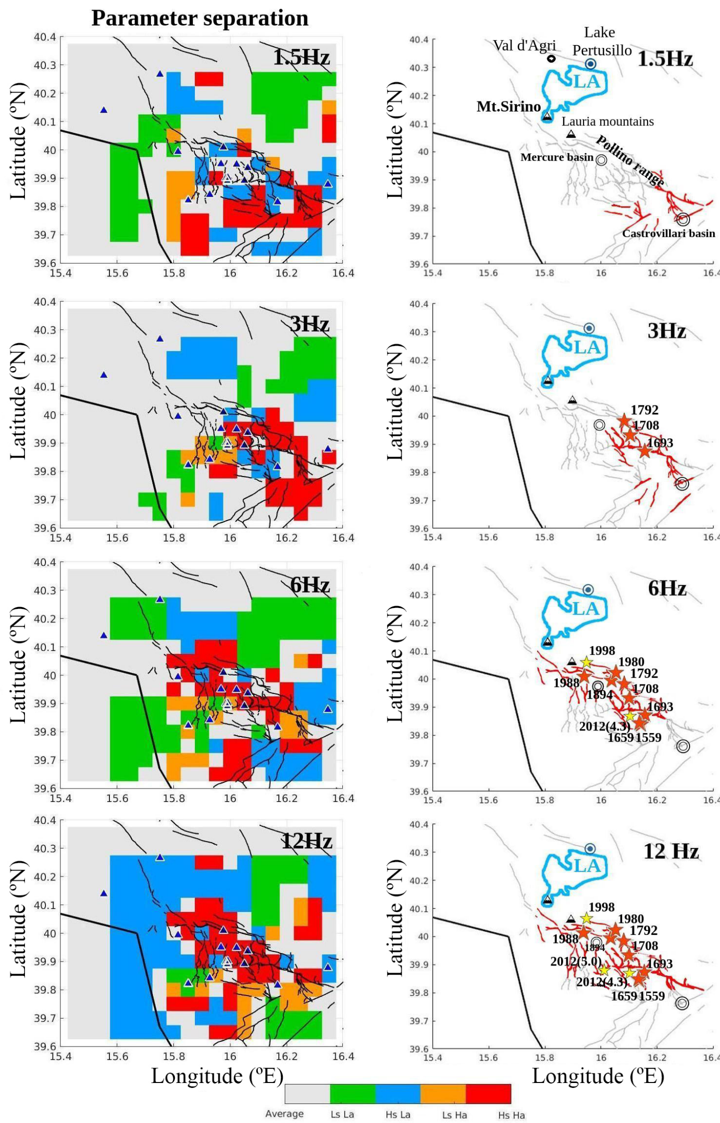
Parameter separation
1.5Hz
3Hz
6Hz
12Hz
Latitude (ºN)
Longitude (ºE)
Val d'Agri
Lake Pertusillo
LA
Mt.Sirino
Lauria mountains
Mercure basin
Pollino range
Castrovillari basin
1792
1708
1693
1998
1980
1988
1894
2012(4.3)
2012(5.0)
1659
1559
12 Hz
Average
Ls La
Hs La
Ls Ha
Hs Ha

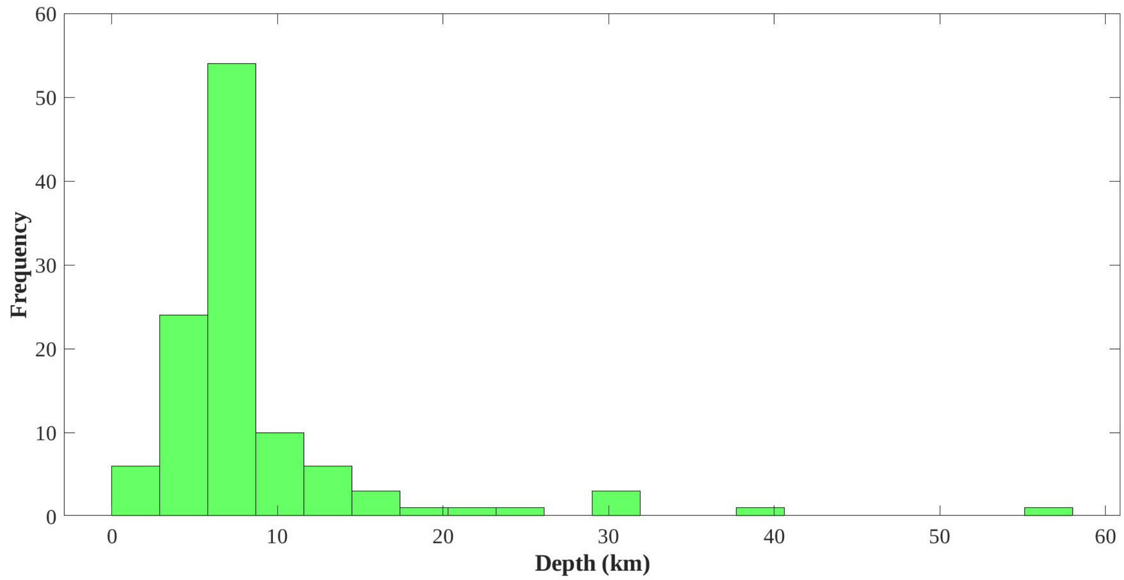
Frequency
Depth (km)
0
10
20
30
40
50
60
0
10
20
30
40
50
60

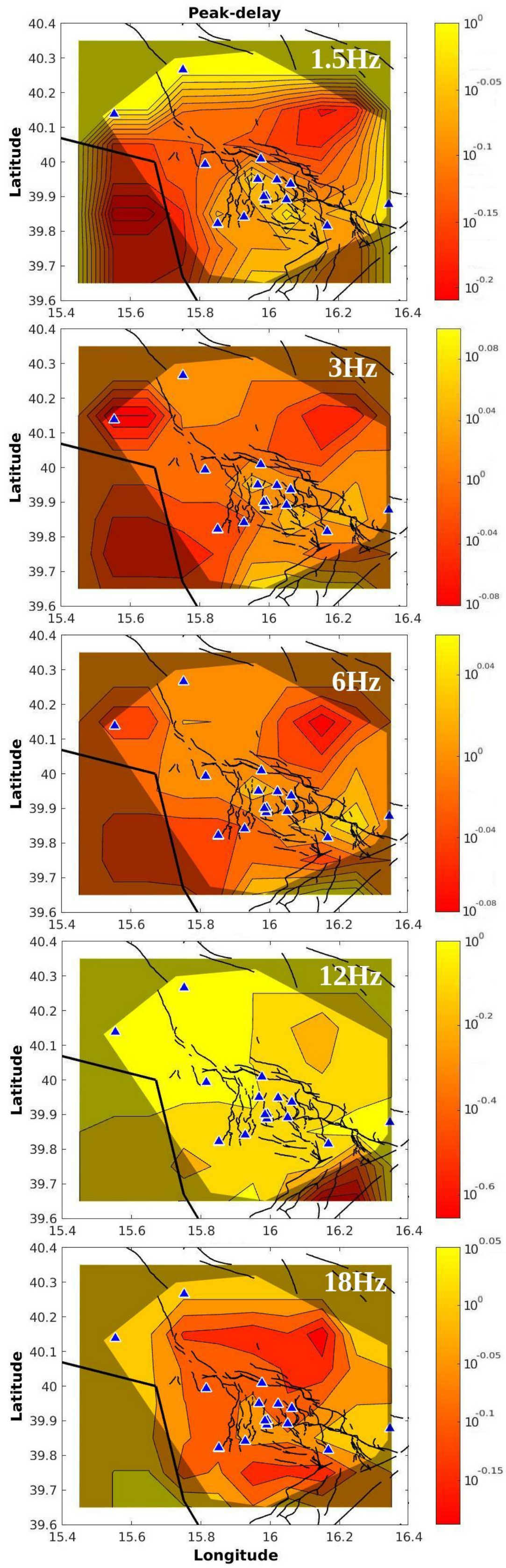

Peak-delay
1.5Hz
3Hz
6Hz
12Hz
18Hz
Latitude
Longitude

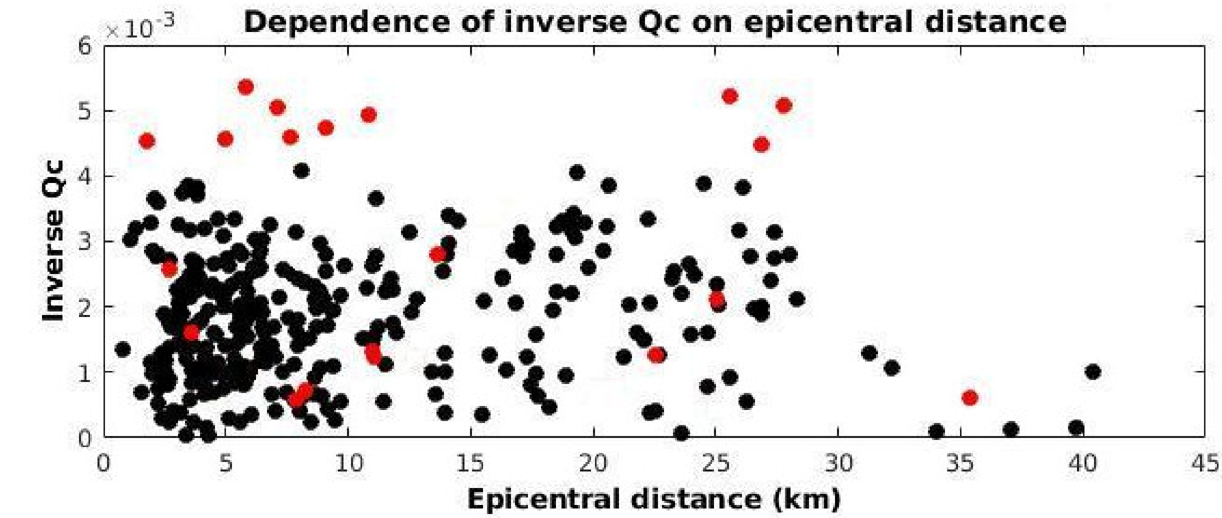
Dependence of inverse Qc on epicentral distance
×10^-3
Inverse Qc
Epicentral distance (km)

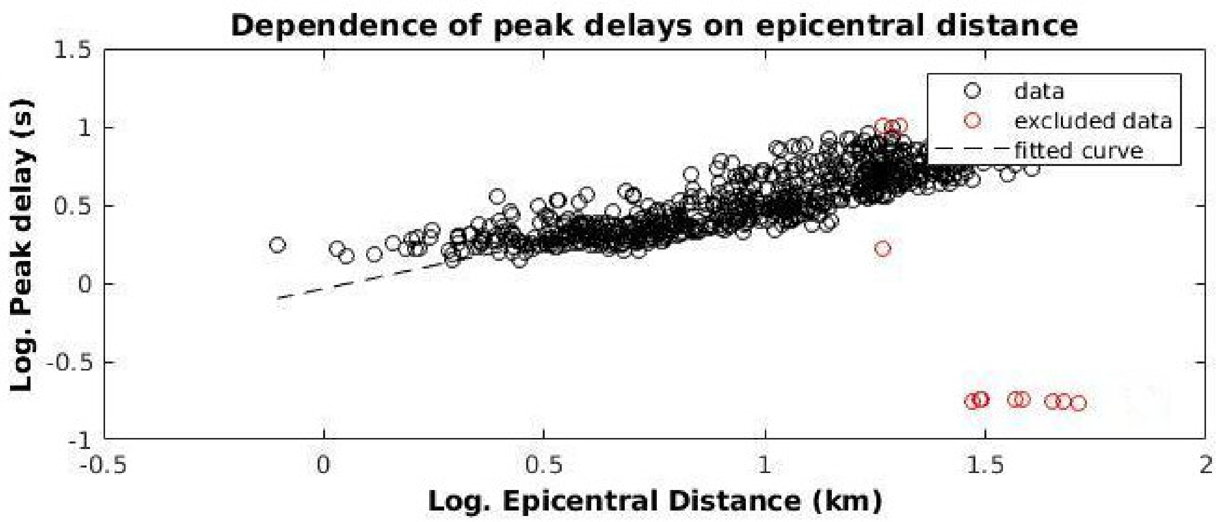
Dependence of peak delays on epicentral distance
data
excluded data
fitted curve
Log. Peak delay (s)
Log. Epicentral Distance (km)

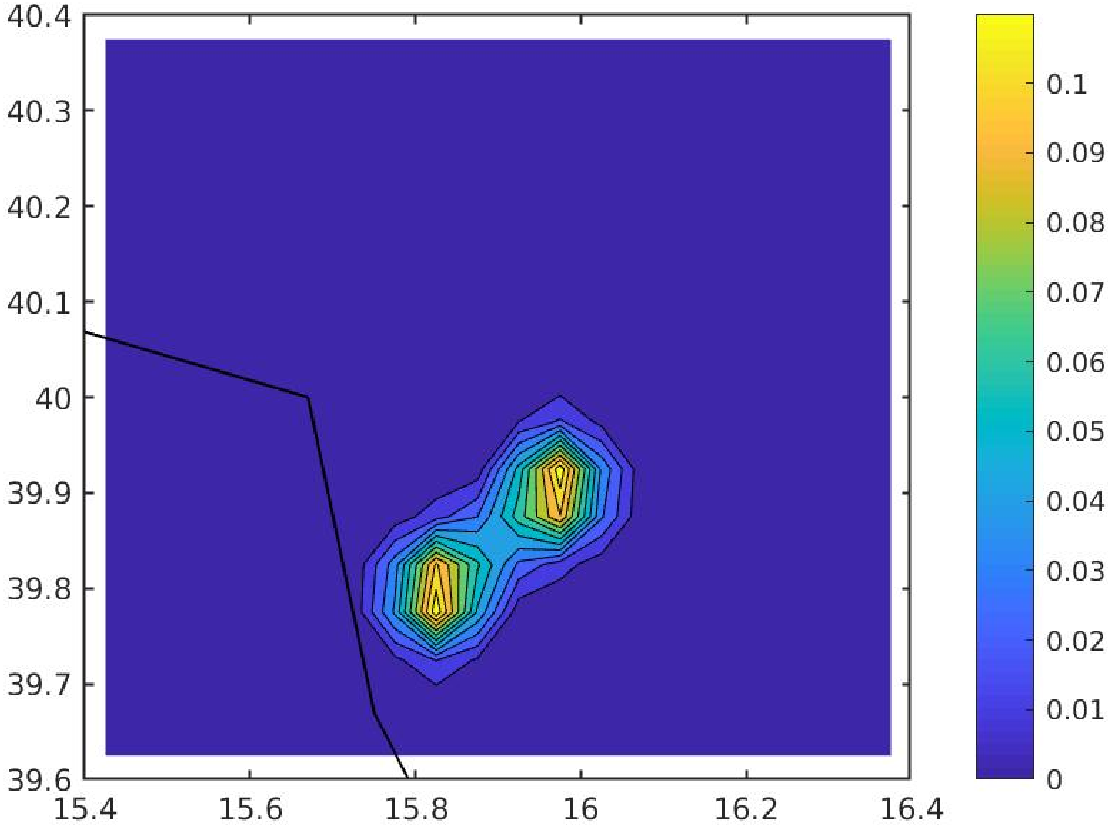
40.4
40.3
40.2
40.1
40
39.9
39.8
39.7
39.6
15.4
15.6
15.8
16
16.2
16.4
0.1
0.09
0.08
0.07
0.06
0.05
0.04
0.03
0.02
0.01
0

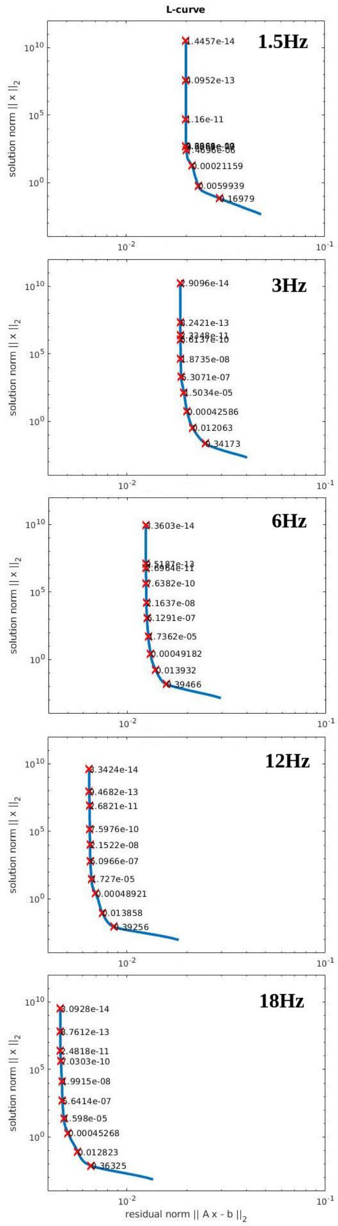
L-curve
1.5Hz
3Hz
6Hz
12Hz
18Hz
solution norm || x ||2
residual norm || A x - b ||2
10^-2
10^-1
10^0
10^5
10^10
.4457e-14
.0952e-13
.16e-11
.00021159
.0059939
.16979
.9096e-14
.2421e-13
.8735e-08
.3071e-07
.5034e-05
.00042586
.012063
.34173
.3603e-14
.6382e-10
.1637e-08
.1291e-07
.7362e-05
.00049182
.013932
.39466
.3424e-14
.4682e-13
.6821e-11
.5976e-10
.1522e-08
.0966e-07
.727e-05
.00048921
.013858
.39256
.0928e-14
.7612e-13
.4818e-11
.0303e-10
.9915e-08
.6414e-07
.598e-05
.00045268
.012823
.36325

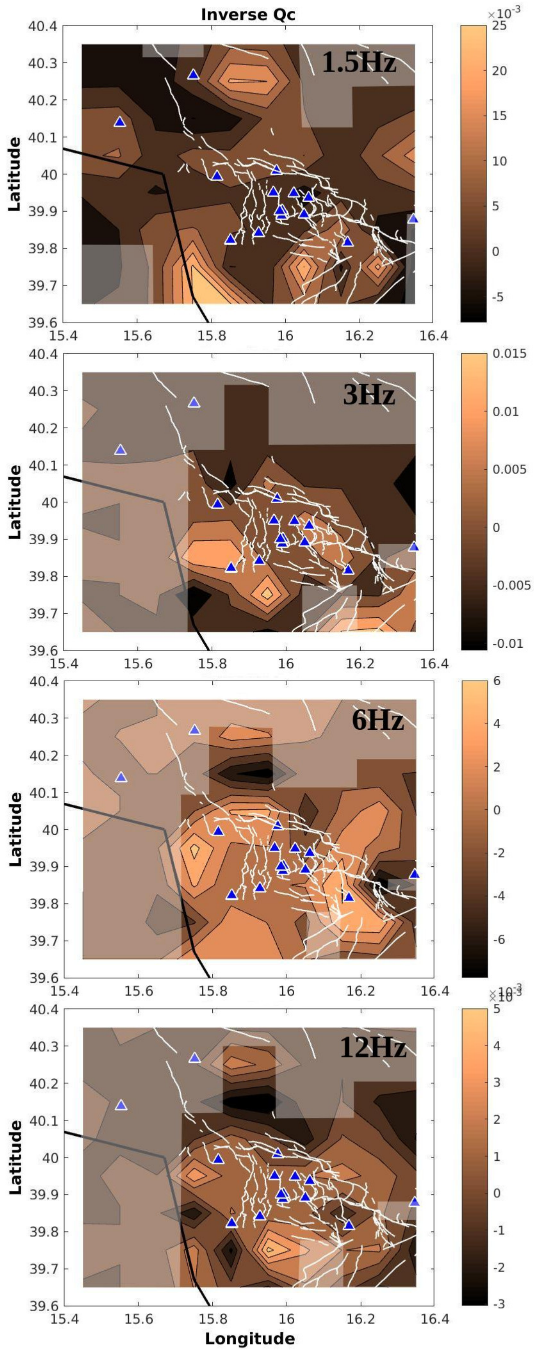
Inverse Qc
1.5Hz
3Hz
6Hz
12Hz
Latitude
Longitude
40.4
40.3
40.2
40.1
40
39.9
39.8
39.7
39.6
15.4
15.6
15.8
16
16.2
16.4
×10-3
25
20
15
10
5
0
-5
0.015
0.01
0.005
0
-0.005
-0.01
6
4
2
0
-2
-4
-6
×10-3
5
4
3
2
1
0
-1
-2
-3

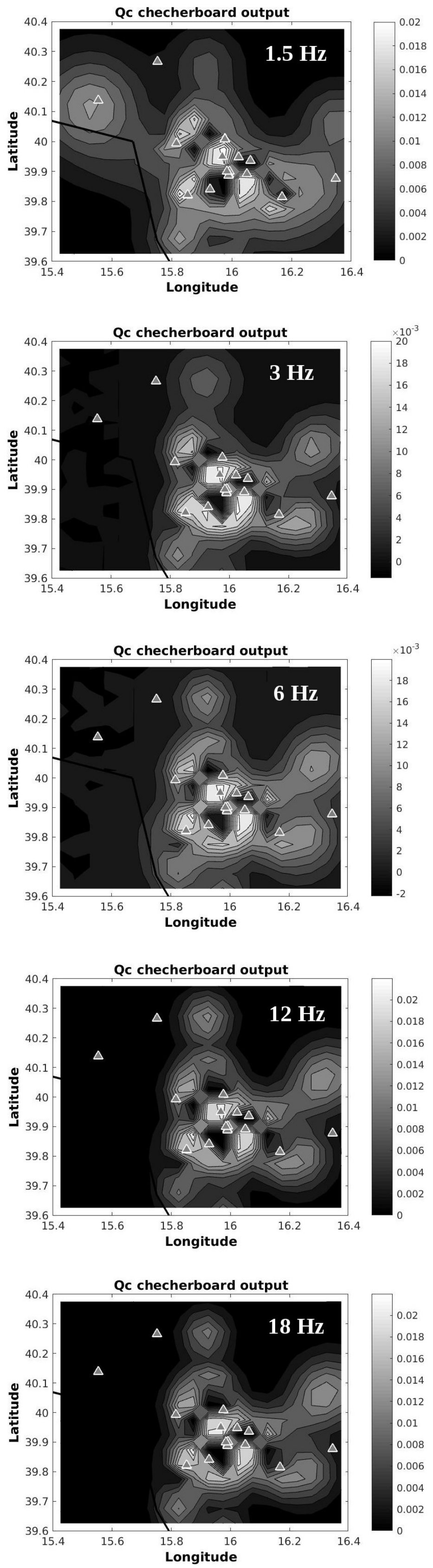
Qc checherboard output
1.5 Hz
Latitude
Longitude
Qc checherboard output
3 Hz
×10-3
Latitude
Longitude
Qc checherboard output
6 Hz
×10-3
Latitude
Longitude
Qc checherboard output
12 Hz
Latitude
Longitude
Qc checherboard output
18 Hz
Latitude
Longitude

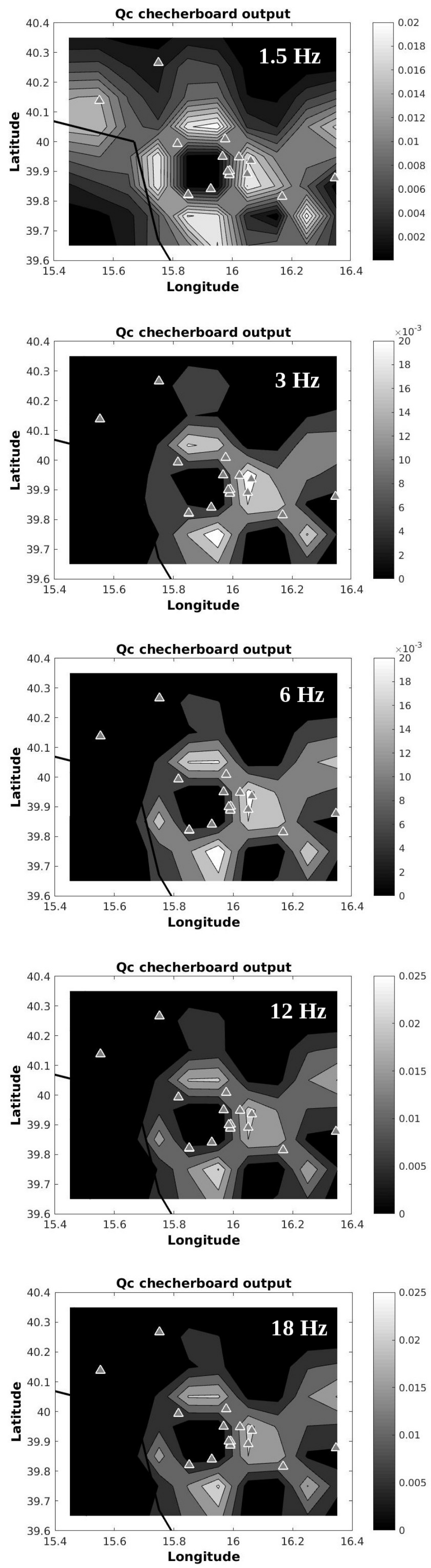
Qc checherboard output
1.5 Hz
Latitude
Longitude
Qc checherboard output
3 Hz
Latitude
Longitude
×10⁻³
Qc checherboard output
6 Hz
Latitude
Longitude
×10⁻³
Qc checherboard output
12 Hz
Latitude
Longitude
Qc checherboard output
18 Hz
Latitude
Longitude

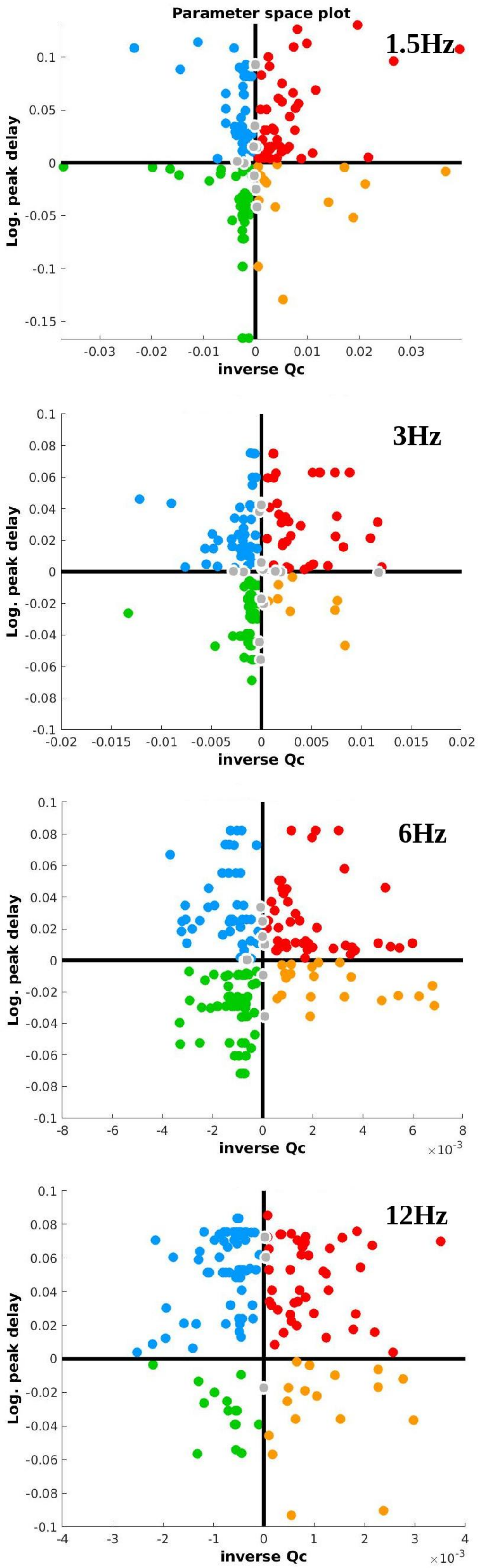
Parameter space plot
1.5Hz
3Hz
6Hz
12Hz
Log. peak delay
inverse Qc
×10^-3

Highlights of the manuscript "Scattering and absorption imaging of a highly fractured fluid-filled seismogenetic volume in a region of slow deformation"

- Multi-frequency maps of faults in the Pollino low-strain region

- High-scattering and high-absorption fluid-filled fractures activate seismogenic faults

- Small fracture networks healed in areas of historical seismicity and weremblocked NW by the Mount Sirino carbonates.